Mathematics

https://www.aimspress.com/journal/Math

AIMS Mathematics, 11(7): 22543–22575.
DOI: 10.3934/math.2026911
Received: 08 June 2026
Revised: 13 July 2026
Accepted: 16 July 2026
Published: 27 July 2026

Research article

Heat and mass transfer in gold nanoparticle-enhanced synovial fluid for biomedical applications: a Carreau-Yasuda study

Bader Saad Alshammari[1], **Shahid Hasnain**[2,*] **and Muhammad Saqib**[3]

[1] Department of Mathematics, Northern Border University, Arar 73222, Saudi Arabia
[2] Department of Mathematics, University of Chakwal, 48800, Pakistan
[3] Department of Mathematics, Khwaja Fareed University of Engineering and Information Technology (KFUEIT), Rahim Yaar Khan, 64200, Pakistan

* **Correspondence:** Email: shahidqa32@gmail.com.

Abstract: Osteoarthritis affects more than 500 million people worldwide, yet existing viscosupplements suffer from rapid clearance and poor cartilage penetration. This study investigates how the coupled effects of viscous dissipation, thermophoretic migration, magnetic induction, and porous absorption govern the spatial distribution of gold nanoparticles injected into the osteoarthritic knee joint. A finite volume solver is developed for flow through a wavy, porous channel with a second-order velocity slip condition at the cartilage surface, incorporating a temperature and concentration-dependent Carreau-Yasuda viscosity, an absorption term in the concentration equation, and the full magnetic induction equation. The results reveal that each transport process is governed by a distinct mechanism: thermal buoyancy and surface slip shape the velocity field, viscous dissipation controls the temperature distribution, and thermophoresis provides a means of actively guiding nanoparticles. Most significantly, cartilage absorption emerges as the dominant barrier to effective drug delivery, while the axial pressure gradient is governed by cartilage permeability and fluid rheology, with second-order slip exerting a strong, previously neglected influence on the pressure distribution. These findings establish that nanoparticle absorption and second-order surface slip cannot be neglected in predictive models of synovial joint biomechanics and intra-articular drug delivery.

Keywords: non-Newtonian biofluid; nanofluid transport; finite volume method
Mathematics Subject Classification: 76A05, 92C35

1. Introduction

The knee is among the most heavily loaded joints in the body, routinely carrying compressive forces of three to eight times body weight during walking and stair climbing, yet it does so at friction coefficients of 0.001 - 0.01 that match the best engineered bearings [1,2]. This performance rests almost entirely on the rheology of synovial fluid, a filtrate of blood plasma enriched with high-molecular-weight hyaluronic acid (10^6-10^7 Da) and the surface-active glycoprotein lubricin [3,4]. Together these macromolecules give the fluid a strongly shear-thinning character: its viscosity falls by roughly two orders of magnitude between a joint at rest and one in vigorous motion, which is what allows the same fluid both to bear load and to lubricate [3]. When this balance is disturbed, either by hyaluronidase activity in rheumatoid arthritis, or by the fragmentation of lubricin films in osteoarthritis, contact stress rises, cartilage wears faster, and the joint deteriorates [5,6].

Osteoarthritis (OA) now affects around 500 million people worldwide and ranks among the leading causes of years lived with disability, at an economic cost estimated at one to two percent of GDP in high-income countries [5]. Treatment remains largely palliative. Non-steroidal anti-inflammatory drugs manage pain without slowing the underlying mechanical decline, and conventional viscosupplementation clears from the joint within a few days and penetrates less than 100 μm into cartilage [7]. The use of gold in the joint has a long therapeutic history: Rasmussen et al. [8] reviewed how implanted metallic gold suppresses local inflammation and has been used in rheumatology for decades, evidencing the biocompatibility and inertness of gold in the articular environment. At the nanoscale, Danscher and Rasmussen [9] showed that nanogold and μ gold actively inhibit autoimmune inflammation, indicating that gold particles are not merely passive carriers but can themselves modulate the inflammatory process that drives joint disease. More broadly, nanoparticle carriers can be engineered for disease-specific targeting within the joint: Deng et al. [10] demonstrated multifunctional nanoparticles that deliver a therapeutic payload selectively to inflammatory macrophages and osteoclasts in rheumatoid arthritis, illustrating the functionalization and targeted, sustained release that motivate a nanoparticle strategy. Even a modest gain in delivery efficiency could stretch the dosing interval from monthly to quarterly, with real consequences for adherence and cost. Whether that gain is achievable depends on how the particles move, spread, and are taken up once inside the joint, a question that is, at heart, one of fluid mechanics.

What sets the particle distribution is not any single effect, but the coupled thermofluid state of the joint as a whole. The velocity field carries the particles; cyclic loading dissipates mechanical energy into local heat; the resulting temperature gradients push particles thermophoretically toward cooler regions; and the particle concentration, in turn, alters the effective viscosity of the carrier fluid through the constitutive law [11, 12]. Capturing this two-way exchange between transport and rheology is the central modeling problem we take up here. For the constitutive law we use the generalized Carreau-Yasuda (GCY) model [13], which spans both the low and high-shear viscosity plateaus continuously and, through an independent Yasuda exponent, controls the sharpness of the transition between them. Our formulation goes a step beyond earlier GCY treatments [11,12] by letting the zero-shear viscosity, the infinite-shear viscosity, and the power-law index each depend on both the local nanoparticle concentration and the local temperature.

The fluid-cartilage boundary adds a second layer of difficulty. The articular surface is not a smooth, rigid wall, but a hydrated, porous, glycoprotein-rich layer whose micro-architecture lets the bulk fluid slip over the solid matrix [14,15]. Navier's first-order slip condition has been used in earlier models of biological channel flow [16, 17], but a first-order description is incomplete in a wavy geometry, where the curvature of the near-wall velocity profile carries physical information of its own. We therefore apply a full second-order slip condition at the cartilage surface. As the parametric study shows, the second-order term is not a small correction; over the range examined it is the single most influential parameter in the model.

Because synovial fluid is weakly conducting ($\sigma \approx 0.5$–1.0 S/m through its Na^+, K^+, and Cl^- content), an applied magnetic field interacts with the flow through a Lorentz coupling [18]. Most MHD bio-flow studies stop at a prescribed external body force. We instead keep the full magnetic induction equation and solve for the motion-induced azimuthal field directly. Doing so uncovers a link between a mechanical surface property which is slip and an electromagnetic output, the induced field, that does not appear to have been reported for synovial fluid, and that points to a practical possibility: inferring cartilage-surface condition from a non-invasive magnetic measurement.

Thermal regulation is a further effect that most joint models leave out. Cartilage is avascular and aneural, so it depends on the convective-diffusive movement of synovial fluid for nutrients and waste clearance [19]. Cyclic loading dissipates energy as heat, and even small temperature rises are enough to upregulate catabolic metalloproteinases and accelerate proteoglycan loss [19, 20]. Suspended nanoparticles add their own thermal contributions through Brownian micro-convection and thermophoresis, both of which we retain through the Buongiorno two-phase framework [21–23].

A final new ingredient is an absorption term for the uptake of nanoparticles by the cartilage matrix. Existing nanoparticle-transport models for biological channels treat concentration as governed by diffusion and thermophoresis alone, with no route for mass to leave the fluid and enter the surrounding tissue [7,12,24,25]. That is not physiological: AuNPs injected into the joint do not circulate indefinitely but are steadily adsorbed by the glycoprotein matrix and the interstitial collagen of the cartilage. We represent this by adding a first-order absorption sink to the dimensionless concentration equation; its effect on wall-normal mass transfer, and hence on delivery efficiency, is quantified in the analysis section.

The full system, momentum, energy, nanoparticle concentration with absorption, and magnetic induction, is solved with a Python finite-volume solver built on NumPy, SciPy, and Matplotlib, giving a transparent and reproducible alternative to proprietary multiphysics codes [26, 27]. Under the long-wavelength lubrication approximation ($\delta = a_2/\lambda \ll 1$), the system reduces to a set of coupled ordinary differential equations at each axial station. For benchmarking, we also implement two simpler viscosity laws, a concentration-enhanced viscoelastic model (Model II), and a concentration-modulated shear-thickening model (Model III), and compare all three against Ramadan et al. [28]; every physical conclusion, however, is drawn from the generalized Carreau-Yasuda model (Model I).

Novelty and key contributions:

The present work builds directly on the synovial nanofluid model of Ramadan et al. [28], which examines gold-nanoparticle transport in an irregular channel under an induced magnetic field. That study, along with the broader Carreau-Yasuda nanofluid literature it draws from [11, 12], rests on several simplifying assumptions: a first-order Navier slip condition, a fixed-coefficient viscosity law, a concentration equation limited to diffusion and thermophoresis, and a magnetic formulation that resolves the field but decouples it from the wall state. Our model departs from this framework on four concrete points, and it is the synergy among them, rather than any single modification, that defines the novelty.

First, we replace the conventional first-order slip with a full second-order condition that preserves near-wall velocity curvature, a term typically neglected, yet in this wavy geometry it governs the flow response and dominates porous drag and magnetic forces by an order of magnitude. In a straight channel the effect would be marginal; in an undulating one, it is not. Second, the Carreau-Yasuda viscosity is fully coupled to the local thermochemical state. Unlike prior studies that treat zero-shear viscosity, infinite-shear viscosity, and the power-law index as constants, we allow all three parameters to evolve with concentration and temperature. This bidirectional coupling produces velocity and temperature fields that measurably differ from any fixed-property prediction. Third, for the first time in a synovial channel model, a nanoparticle absorption term is introduced. A first-order sink in the concentration equation accounts for continuous particle uptake by the cartilage matrix, an effect omitted in earlier formulations yet critical for determining the fraction of an injected dose that reaches target tissue. This term also provides a direct lever for design: modifying surface properties to slow absorption directly alters bioavailability. Fourth, solving the full induction equation reveals selective sensitivity, the field responds strongly to slip and magnetic Reynolds number but remains nearly indifferent to thermal and concentration parameters. This pattern, unreported for synovial fluids, positions the induced field as a potential non-invasive probe of cartilage-surface condition.

Complementing these advances, we provide the first quantitative breakdown of thermal sources in a fully coupled synovial nanofluid, isolating the distinct contributions of viscous dissipation, Brownian motion, and thermophoresis to intra-articular temperature rise. Collectively, these modeling enhancements and the resulting apportionment establish quantitative benchmarks, presented in the analysis section, against which future experimental and numerical studies can be evaluated. Henceforth, these advancements, further demonstrate that second-order slip, matrix absorption, and self-consistent field induction are not minor refinements, but essential physics for credible synovial joint biomechanics.

2. Physical configuration and modelling framework

2.1. Geometric description of the knee joint domain

The computational domain is the annular channel in a cylindrical coordinate system (R, Z), created by two concentrically placed vertical cylinders. This geometry is a knee joint instrumented for endoscopic or catheter-based intervention, where the outer surface of the synovial cavity is the articular cartilage surface and the inner surface is a smooth surface of constant radius, $R_1 = c_1$. The inner wall is assumed to be smooth, mechanically stiff, and electrically insulating. A physiologically motivated bi-harmonic profile is used to describe the outer wall at mean radius c_2 that captures the spatial undulations caused by cartilage micro-topography and cyclic joint deformations:

$$R_2 = c_2 + \delta_1 \cos(\frac{\gamma_1 \pi}{\lambda}(Z - ct)) + \delta_2 \cos(\frac{\gamma_2 \pi}{\lambda}(Z - ct)). \tag{2.1}$$

In this case, the two superimposed wave components' amplitudes are δ_1 and δ_2, the dimensionless wave-number parameters are γ_1 and γ_2, the axial wavelength is λ, the propagation speed of the surface deformation wave is c, and t represents time. This dual-harmonic representation, validated with imaging data from cadaveric knee cartilage [28–30], produces qualitatively richer flow patterns than single-harmonic walls, specifically, the bolus-like asymmetric flow pattern that dominates the trapping, and retention of nanoparticles in the joint space (see Figure 1). A wave-fixed reference frame (r, z) is used to remove the time dependence and describe the flow in a geometrically stationary domain by the transformation $r = R$, $z = Z - ct$ and $p = P$. The velocity components in the moving frame are defined by $u = U_R$, and $w = U_Z - c$. This transformation transforms the unsteady peristaltic problem into a steady problem, which significantly reduces the computational cost and retains all the important physics [31, 32] for the case when the domain length is an integer multiple of the wavelength.

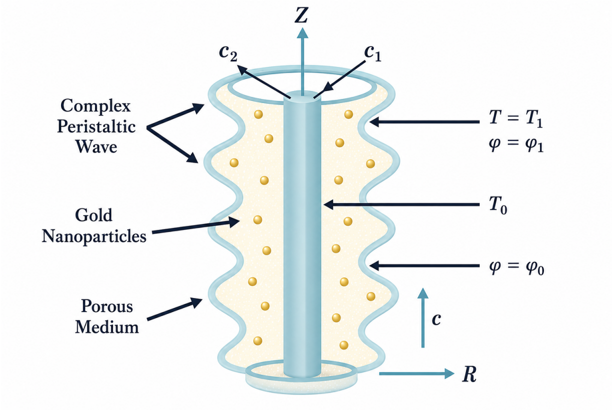

Figure 1. Model configuration in cylindrical coordinates [28].

2.2. *Physical modeling assumptions*

The mathematical model is based on the following assumptions which are based on physical principles:

- A nanofluid of electrically conductive synovial fluid with gold nanoparticles (GNPs) in volume fraction φ flows in an incompressible manner through a permeable annulus, representative of the knee-joint cavity [1, 5].
- Non-Newtonian shear-thinning behavior in the form of a Carreau-Yasuda model including full concentration and temperature dependence. Two simplified models (Models II and III) are implemented only for benchmarking purposes against Ramadan et al. [28].
- Under the long-wavelength lubrication approximation $\delta = c_2/\lambda \ll 1$ and in the steady flow frame in the wave-fixed frame in the low Reynolds number regime ($R_e \ll 1$), which is consistent with the physiological transport of synovial fluid [**?**, 30].
- A uniform axial magnetic field H_0 is applied externally and the finite electrical conductivity σ produces an induced field which is solved by using the complete magnetic induction equation. Under quasi-static MHD conditions, free-charge and displacement-current are have with negligible effects [18].
- The cartilage surface is modeled using a second-order velocity slip condition, where both the linear slip coefficient β and the curvature slip coefficient ξ [14, 15] are retained.
- The gravitational settling of the particles is negligible at the relevant particle size, and the transport of nanoparticles is modeled using the Buongiorno two-phase model [21], which incorporates Brownian diffusion and thermophoresis.
- The energy equation includes viscous dissipation, internal heat generation/absorption, Brownian micro-convective heating, and thermophoretic energy flux. The tangential induced field on both walls is zero, thus both walls are electrically non conducting.

Magnetohydrodynamic parameters: Rather than prescribing a Lorentz force, we solve the full induction equation and treat the magnetic Reynolds number R_{e_m} and the Strommer number S as independent control parameters, varied across a representative range to expose the flow field coupling structure. Physiologically, $R_{e_m} = \mu_e \sigma U c_2$ is small; thus, induced field results are interpreted mechanistically, as a characterisation of sensitivity to flow and slip, not as absolute in vivo magnitudes. This follows the parametric convention of the peristaltic MHD-nanofluid literature [18, 28], and it is precisely this sensitivity pattern, not the field strength.

Absorption term: Nanoparticle uptake by the cartilage matrix is modeled as a first-order sink $-\gamma_{\text{abs}}\,\phi$ in the concentration equation, the dilute, unsaturated limit of Langmuir-type adsorption. This is justified here because volume fractions are low and the matrix remains far from saturation over the relevant transport timescale [7]. Near saturation, the uptake would plateau, requiring a nonlinear sink; the present linear form should be read as a leading-order approximation valid in the dilute regime.

Slip coefficients: The first and second-order slip coefficients β and ξ are assigned representative dimensionless values consistent with the porous, glycoprotein rich cartilage interface [14,15]. Since the effective curvature coefficient ξ for articular cartilage lacks direct experimental constraint, we treat it parametrically rather than fixing it. Its strong influence on the flow, established in the analysis section, emerges as a central finding and justifies this approach.

3. Mathematical formulations

3.1. Governing system

Using the previously defined geometric configuration and coordinate transformation, the governing rheological relations are reformulated within the wave-fixed reference frame. The established geometric scaling, together with the transformation from the stationary frame to the moving frame, enables the constitutive equations to be expressed as

$$\nabla^* \cdot \mathbf{V}^* = 0, \tag{3.1}$$

$$\begin{cases} \rho_t \left(\dfrac{\partial \mathbf{V}^*}{\partial t^*} + (\mathbf{V}^* \cdot \nabla^*)\mathbf{V}^* \right) = -\nabla^* P^* + 2\nabla^* \cdot (\mu^*(\varphi^*, D^*)D^*) - \dfrac{\nu}{k_1}\mathbf{V}^* + \mu_e(\nabla^* \times \mathbf{H}^*) \times \mathbf{H}^* + \mathbf{F}^*_{buoyancy}, \\ \mathbf{F}^*_{buoyancy} = \left[\rho_g \varphi^* + (1-\varphi^*)(\rho_t(1-\beta_T(T^*-T_0))) \right] g, \end{cases} \tag{3.2}$$

$$\begin{cases} (\rho c)_t \left((\mathbf{V}^* \cdot \nabla^*)T^* + \dfrac{\partial T^*}{\partial t^*} \right) = k_T \nabla^{*2} T^* + \left[D_B(\nabla^* T^* \cdot \nabla^* \varphi^*) + \left(\dfrac{D_T}{T_m} \right)(\nabla^* T^* \cdot \nabla^* T^*) \right] (\rho c)_p + \mathbf{F}^*_0, \\ \mathbf{F}^*_0 = Q_0 + \mu \left[2\left(\dfrac{\partial U^*_R}{\partial R^*} \right)^2 + 2\left(\dfrac{U^*_R}{R^*} \right)^2 + 2\left(\dfrac{\partial U^*_Z}{\partial Z^*} \right)^2 + 2\left(\dfrac{\partial U^*_Z}{\partial R^*} + \dfrac{\partial U^*_R}{\partial Z^*} \right)^2 \right], \end{cases} \tag{3.3}$$

$$\frac{\partial \varphi^*}{\partial t^*} + (\mathbf{V}^* \cdot \nabla^*)\varphi^* = D_B \nabla^{*2}\varphi^* + \left(\frac{D_T}{T_m} \right) \nabla^{*2} T^* - \Lambda \varphi^* + S_0. \tag{3.4}$$

The conducting synovial nanofluid is modeled based on classical magnetohydrodynamics in the present analysis. Owing to the influence of free electric charges and magnetic field strengths on the physiological state being relatively small, the physiological values are relatively low in both aspects.

It is assumed that the displacement current terms are negligible. In such quasi-static situation, the electromagnetic field changes immediately with the fluid flow, in which case the governing equations are simplified to that of magnetohydrodynamics:

$$\begin{cases} \nabla^* \cdot \mathbf{E}^* = 0,\ \nabla^* \cdot \mathbf{H}^* = 0,\ \nabla^* \times \mathbf{H}^* = \mathbf{J}^*, \\ \nabla^* \times \mathbf{E}^* = \mu_e \dfrac{\partial \mathbf{H}^*}{\partial t^*},\ \mathbf{J}^* = \sigma \left(\mathbf{E}^* + \mu_e \left(\mathbf{V}^* \times \mathbf{H}^* \right) \right), \end{cases} \tag{3.5}$$

by utilizing Eq (3.5), the induction equation can be expressed as

$$\frac{\partial \mathbf{H}^*}{\partial t^*} = \nabla^* \times (\mathbf{V}^* \times \mathbf{H}^*) + \frac{1}{\mu_e \sigma} \nabla^{*2} \mathbf{H}^*. \tag{3.6}$$

3.2. Long wavelength approximation and dimensionless reduction of the governing system

In fluid dynamics, the long wavelength approximation is used in situations where the length of the channel along the direction of flow is much greater than the width or radius of the channel. The geometry varies slowly; in other words, any variation is over a distance much longer than across the channel. Mathematically, this situation is represented by a small parameter termed as the aspect ratio, which is c_2/λ, where c_2 is the transverse dimension of the channel (such as the tube radius) and λ is the characteristic axial wavelength of the variation of the channel. From the point of view of synovial joint lubrication, the undulation length of the cartilage surface is l and the thickness of the gap between the cartilage is c_2. If the joint gap δ is small relative to the wavelength of the wavy surface, then terms that represent axial changes are negligibly small relative to those representing transverse changes; this is a good approximation for many biological flows where δ is small compared to the wavelength of the wavy surface. This observation results in a drastic reduction of the governing equations. This approximation is only truly useful when used in conjunction with variables that are dimensionless, as defined in Table 1.

Table 1. Dimensionless form of variables.

Dimensionless variable	**Definition**	**Dimensionless variable**	**Definition**
		Geometric & kinematic variables	
δ	c_2/λ	$r^\star$	R/c_2
$z^\star$	Z/λ	$t^\star$	tc/λ
$R_1^\star$	$R_1/c_2 = \epsilon$	$R_2^\star$	R_2/c_2
$\eta_1^\star$	η_1/c_2	$\eta_2^\star$	η_2/c_2
		Velocity & magnetic field variables	
$u^\star$	$\lambda U_R/(cc_2)$	$w^\star$	U_Z/c
$h_r^\star$	H_R/H_0	$h_z^\star$	H_Z/H_0
		Thermal & concentration variables	
θ	$\dfrac{T - T_0}{T_1 - T_0}$	ϕ	$\dfrac{\varphi - \varphi_0}{\varphi_1 - \varphi_0}$
$p^\star$	$c_2^2 P/(c\lambda\mu_0)$	$\mu^\star$	μ/μ_0

Continued on next page

Dimensionless variable	Definition	Dimensionless variable	Definition
	Dimensionless flow parameters		
R_e	$c\rho c_{outer}/\mu_0$	R_{e_m}	$c\sigma\mu_e c_2$
S^2	$\mu_e H_0^2/(c^2\rho_f)$	k	c_2^2/k_1
G_r	$\dfrac{g\beta_T\rho_f c_{outer}^2(T_1-T_0)}{\mu_0 c}$	G_f	$\dfrac{g(\rho_P-\rho_f)c_{outer}^2(\varphi_1-\varphi_0)}{\mu_0 c}$
N_b	$\dfrac{(\rho c)_p D_B(\varphi_1-\varphi_0)}{k_T}$	N_t	$\dfrac{(\rho c)_p D_T(T_1-T_0)}{T_m k_T}$
P_r	$\mu_0 c_p/k_T$	E_c	$\dfrac{c^2}{c_p(T_1-T_0)}$
L_e	$\dfrac{\mu_0}{\rho_f D_B}$	ω_e^2	$\dfrac{\gamma^2c^2}{c_2^2}$
α	$a(\varphi_1-\varphi_0)$	A_1	$\delta_1\varphi_1$
A_2	$\delta_2\varphi_1$	m_∞	$\mu_{\infty0}/\mu_{00}$
$\beta_1^\star$	$\beta_1(T_1-T_0)$	$\beta_2^\star$	$\beta_2(T_1-T_0)$
$\beta_3^\star$	$\beta_3(T_1-T_0)$	ω_i	$\lambda_0 c/c_2$

A complete list of symbols, definitions, and SI units for all variables is provided in Table 2. For example, the dimensionless radial coordinate $r^\star = R/c_2$, the dimensionless axial coordinate $z^\star = Z/\lambda$, and the aspect ratio $\delta = c_2/\lambda$ are not simply arbitrary definitions, but they have been carefully chosen to illustrate the relative magnitudes of different physical effects. Each of the terms in the full Navier-Stokes energy, concentration, and magnetic induction equations scales naturally with a suitable power of δ when we substitute the dimensionless variables. Any terms that are raised to higher powers of δ (e.g., δ^2 or δ^3) get correspondingly smaller. If only the leading-order terms (those of order δ^0 or δ^1) are kept in the original two-dimensional system (or three-dimensional system), then the original system becomes a much simpler quasi one-dimensional form.

Table 2. Symbols, definitions, and SI units.

Symbol	Definition	SI unit	Symbol	Definition	SI unit
		Velocity & flow field			
u, w	Velocity components in wave frame	m/s	R_e	Reynolds number	-
$\mathbf{V}$	Velocity vector	m/s	U_R^*, U_Z^*	Velocity at fixed frame	m/s
c	Wave propagation velocity	m/s	λ	Wavelength	m
		Geometric parameters			
c_1, c_2	Inner/outer radii	m	ϵ	Radius ratio	-
ϵ_1, ϵ_2	Wave amplitudes	m	α_1, α_2	Wave parameters	-
R	Radial coordinate	m	Z	Axial coordinate	m

Continued on next page

Symbol	Definition	SI unit	Symbol	Definition	SI unit
		Pressure & flow dynamics			
p	Pressure	Pa	k	Porous parameter	-
k_1	Permeability of porous medium	m^2	β, ξ	Slip parameters	-
δ	Wave number	-	n	Shear-thinning index	-
		Thermal parameters			
T	Local temperature	K	T_m	Fluid mean temperature	K
T_0, T_1	Reference temperatures	K	Q	Heat source parameter	-
Q_0	Heat source strength	W/m^3	P_r	Prandtl number	-
E_c	Eckert number	-	Φ	Dissipation function	W/m^3
β_T	Thermal expansion coefficient	1/K	$\beta_1, \beta_2, \beta_3$	Temperature sensitivity coefficients	1/K
$(\rho c)_P$	Nanoparticle heat capacity	J/(kg·K)	k_T	Thermal conductivity	W/(m·K)
		Mass transfer & nanoparticle parameters			
φ	Nanoparticle volume fraction	-	φ_0, φ_1	Reference volume fractions	-
D_B	Brownian diffusion coefficient	m^2/s	D_T	Thermophoretic coefficient	m^2/(s·K)
N_b	Brownian motion parameter	-	N_t	Thermophoresis parameter	-
L_e	Lewis number	-	δ_1, δ_2	Linear concentration coefficients	-
A_1, A_2	Concentration coupling parameters	-	γ_{abs}	Absorption coefficient	-
		Magnetohydrodynamic (MHD) parameters			
h_r, h_z	Induced magnetic field components	T	H_0	Applied magnetic field strength	T
R_{e_m}	Magnetic Reynolds number	-	S	Strouhal (Strommer) number	-
$\mathbf{E}$	Induced electric field	V/m	J	Current density	A/m^2
σ	Electrical conductivity	S/m	μ_e	Magnetic permeability	H/m
		Fluid properties & material constants			
ρ_f	Fluid density	kg/m^3	ρ_P	Nanoparticle density	kg/m^3
μ	Dynamic viscosity	Pa·s	μ_0	Reference viscosity	Pa·s

Continued on next page

Symbol	Definition	SI unit	Symbol	Definition	SI unit
$\mu_{\infty 0}$	Infinite shear viscosity	Pa·s	μ_{00}	Zero shear viscosity	Pa·s
m_∞	Viscosity ratio ($\mu_{\infty 0}/\mu_{00}$)	-	γ, α, μ_0	Material constants	Depends
λ_0, γ_0	Relaxation times	s	g	Gravitational acceleration	m/s^2
G_r	Thermal Grashof number	-	G_f	Density Grashof number	-
ω_e, ω_i	Weissenberg numbers	-	a	Yasuda exponent	-

The radial pressure gradient, for example, is zero across the channel (along its length), so that the pressure in the channel does not change across the channel. The axial momentum equation becomes an ordinary differential equation along the radial coordinate r and the axial coordinate z is only a parameter in the local channel geometry $R_2(z)$. The equations of energy, concentration, and magnetic induction are similarly reduced to ordinary differential equations in r at each cross-section z. The use of these dimensionless variables in Table 1 and the long wavelength condition $\delta \ll 1$ allows this to be transformed into a computationally tractable system with efficient solution using standard finite-volume methods.

$$\frac{\partial h_r}{\partial r} + \frac{h_r}{r} = 0, \tag{3.7}$$

$$\frac{\partial p}{\partial r} = 0, \tag{3.8}$$

$$\frac{\partial p}{\partial z} = 2\left[\frac{\mu}{r}\frac{\partial}{\partial r}\left(r\frac{\partial w}{\partial r}\right) + \frac{\partial \mu}{\partial r}\frac{\partial w}{\partial r}\right] - k\mu w + S^2 R_e \frac{\partial h_z}{\partial r}\left(\frac{R_2}{r} + h_r\right) - G_r\theta + G_f\phi, \tag{3.9}$$

$$\frac{\partial^2\theta}{\partial r^2} + \frac{1}{r}\frac{\partial\theta}{\partial r} + N_b\frac{\partial\phi}{\partial r}\frac{\partial\theta}{\partial r} + N_t\left(\frac{\partial\theta}{\partial r}\right)^2 + E_c P_r \mu\left(\frac{\partial w}{\partial r}\right)^2 + Q = 0, \tag{3.10}$$

$$\frac{\partial^2\phi}{\partial r^2} + \frac{1}{r}\frac{\partial\phi}{\partial r} + \frac{N_t}{N_b}\left(\frac{\partial^2\theta}{\partial r^2} + \frac{1}{r}\frac{\partial\theta}{\partial r}\right) - \gamma_{\text{abs}}\phi + S_0 = 0, \tag{3.11}$$

$$\left(\frac{R_2}{r} + h_r\right)\frac{\partial w}{\partial r} = -\frac{1}{R_{e_m}}\left(\frac{1}{r}\frac{\partial}{\partial r}\left(r\frac{\partial h_z}{\partial r}\right)\right). \tag{3.12}$$

Dropping the stars for simplicity, the dimensionless viscosity models are

$$\mu = m_\infty e^{-\beta_2\theta} \; + \; \left[(1 + A_1\phi)e^{-\beta_1\theta} - m_\infty e^{-\beta_2\theta}\right]\left[1 + (\omega_i\,|\dot{\gamma}|)^a\right]^{\frac{n_0(1+A_2\phi)e^{-\beta_3\theta}-1}{a}}, \tag{3.13}$$

$$\mu = (1 + \alpha\phi)\left[1 + n\omega_e^2\left(\frac{\partial w}{\partial r}\right)^2\right], \tag{3.14}$$

$$\mu = \left(1 + \frac{\alpha\phi}{2}\omega_e^2\left(\frac{\partial w}{\partial r}\right)^2\right). \tag{3.15}$$

The boundary conditions are

$$w = 0, \quad h_r = 0, \quad h_z = 0, \quad \theta = 0, \quad \phi = 0, \quad \text{at} \quad r = \epsilon, \tag{3.16}$$

$$w = 1 - \beta\frac{\partial w}{\partial r} - \xi\frac{\partial^2 w}{\partial r^2}, \quad h_r = 0, \quad h_z = 0, \quad \theta = 1, \quad \phi = 1, \tag{3.17}$$
$$\text{at} \quad r = R_2 = 1 + \epsilon_1\cos(\alpha_1\pi z) + \epsilon_2\cos(\alpha_2\pi z).$$

4. Methodology

From a computational standpoint, long wave approximation greatly reduces the numerical complexity of modeling joint mechanics. This reduction uses of efficient numerical methods such as the finite volume method (FVM) or finite element method, which can then be applied to patient-specific geometries reconstructed from imaging data. The core strength of FVM lies in its integral formulation: the governing partial differential equations are expressed in a conservative form and integrated over small, finite-sized control volumes. This ensures that mass, momentum, and energy are conserved locally within each discretized element, a feature that is essential for accurately representing the transport and flow balance within the extremely confined synovial cavity [26, 27, 33, 34]. The governing partial differential equations for velocity w, temperature θ, nanoparticle concentration ϕ, and induced magnetic field h_z are discretized using a cell-centered finite volume method on a uniform axisymmetric grid. For any transported scalar Φ, the steady-state equation after applying the long wavelength approximation can be written in the general form

$$\frac{1}{r}\frac{\partial}{\partial r}\left(r\Gamma_\Phi\frac{\partial\Phi}{\partial r}\right) + (\text{source terms}) = 0, \tag{4.1}$$

where Γ_Φ is the diffusion coefficient specific to each equation: $\Gamma_w = \mu$ for velocity, $\Gamma_\theta = 1/P_r$ for temperature, $\Gamma_\phi = 1$ for concentration, and $\Gamma_{h_z} = 1/R_m$ for the induced magnetic field. Integrating this equation over a control volume of thickness Δr and applying the divergence theorem yields a set of algebraic equations. For a one-dimensional radial grid with N nodes, the discretized equation at interior node i takes the form

$$a_P\Phi_P = a_E\Phi_E + a_W\Phi_W + b, \tag{4.2}$$

where the coefficients are given by

$$a_E = \frac{\Gamma_e\, r_e}{(\Delta r)^2}, \; a_W = \frac{\Gamma_w\, r_w}{(\Delta r)^2}, \; a_P = a_E + a_W + a_{\text{source}}, \; b = S_u\,\Delta V. \tag{4.3}$$

Here, $r_e = (r_i + r_{i+1})/2$ and $r_w = (r_{i-1} + r_i)/2$ are the face radii, Γ_e and Γ_w are the diffusion coefficients interpolated linearly from adjacent cell centers, and $\Delta V = \pi(r_{i+1/2}^2 - r_{i-1/2}^2)$ is the control volume.

The term a_{source} accounts for any linear contributions from sources (e.g., the porous resistance $-k\mu w$ in the momentum equation), while S_u contains all explicit source terms such as buoyancy, magnetic forces, viscous heating, thermophoresis, and the pressure gradient, whereas the boundary conditions are imposed directly.

The resulting system of linear equations is assembled into a sparse matrix A using the scipy.sparse.diags function. Due to the strong coupling between the four fields, viscosity depends on temperature and concentration, the source terms couple all equations, and the system is solved iteratively. At each iteration, the viscosity field is updated based on the current velocity, temperature, and concentration using the appropriate constitutive model (Carreau-Yasuda, viscoelastic, or shear-thickening). The momentum, energy, concentration, and magnetic equations are then solved sequentially using under-relaxation to promote convergence. The iteration continues until the maximum change in any field falls below a tolerance of 10^{-7}.

The linearity of each individual equation (when the source terms are treated explicitly) permits the use of a direct solver without the need for upwind or power-law schemes. The pressure gradient dp/dz, which drives the axial flow, is not an input parameter, but is determined at each axial position z using a direct superposition method: the flow rate q is a linear function of dp/dz, so $dp/dz = (Q_{\text{target}} - Q_{\text{hom}})/Q_{\text{part}}$, where Q_{hom} is the flow rate with $dp/dz = 0$ and Q_{part} is the flow rate with $dp/dz = 1$.

5. Analysis

The effect of the various dimensionless parameters on the velocity $w(r)$, temperature $\theta(r)$, concentration of the nanoparticles $\phi(r)$, induced magnetic field $h_z(r)$, and also on the axial pressure gradient dp/dz is systematically investigated. The goal is to determine the quantitative importance of the physical mechanisms, that is, which parameters are most important in which transport process, at which location, and how the two processes are coupled through the two coupled governing equations. Unless otherwise stated, the baseline parameters are $k = 0.01$, $R_e = 0.1$, $G_r = 3.0$, $\beta = 0.1$, $Pr = 0.7$, $Ec = 0.9$, $N_b = 3.1$, $N_t = 0.1$, $Q = 2.0$, $\gamma_{\text{abs}} = 0.5$, $R_{e_m} = 3.0$, $S = 2.5$, $\omega_e = 0.01$, and $\xi = 0.005$, with a constant flow rate $q = 2.0$ maintained throughout.

5.1. Model validation

The credibility of the present finite volume solver is justified by comparing the present solver results with the benchmark results of Ramadan et al. [28] for the four field variables as shown in Figure 2, and the results are satisfactory.

- **Velocity field:** All the axial velocity profiles shown here under the influence of $G_r = 0.3$ and $G_r = 0.5$ for all the three models, namely Models I, II, and III, are in a good agreement with each other, with the peak value of $w_{\max} \approx 0.30$ at $r \approx 0.9$. The two models (Carreau-Yasuda) give almost exactly the same profile over the entire radial range, with the channel core of Model II being about 0.005 lower than that of Model I; similarly, Model III is slightly lower in the channel center by about 0.005 than the other two models, due to its lower effective viscosity at moderate shear rates.
- **Temperature field:** At low heat absorption ($Q = 0.1$), all three models collapse onto a single monotonically increasing profile spanning $\theta = 0$ at the inner wall to $\theta = 1$ at the outer wall, with inter-model deviation below the line-to-width resolution of the figure. The energy equation is

therefore primarily governed by the source term Q and only weakly by the choice of viscosity model, a physically coherent decoupling that validates the energy equation implementation.

- **Concentration field:** The nanoparticle concentration profiles under the effect of the thermophoresis parameter ($N_t = 0.10, 0.12$) present the most decisive validation result: all six curves are completely superimposed into a single monotonically increasing profile from $\phi = 0$ to $\phi = 1$. This complete collapse confirms that the concentration field is decoupled from macroscopic rheology and that the Brownian thermophoretic diffusion operator, is correctly discretized independently of the velocity field coupling.
- **Induced magnetic field:** It is seen that the induced azimuthal field h_z due to the effects of G_f (5.0, 7.0) possess a physically consistent and clear model hierarchy: Model I has its peak at $h_{z,\max} \approx 0.067$ at $r \approx 0.40$, at which the source term of the magnetic induction equation, namely the radial velocity gradient $\partial w/\partial r$, has its maximum value. The boundary conditions of the electromagnetic field are satisfied exactly at both walls and the zero crossing structure in the outer half of the annulus ($r > 1.1$) is reproduced consistently for all the curves, which is a good sign of exact enforcement of the electromagnetic boundary conditions in all three formulations.

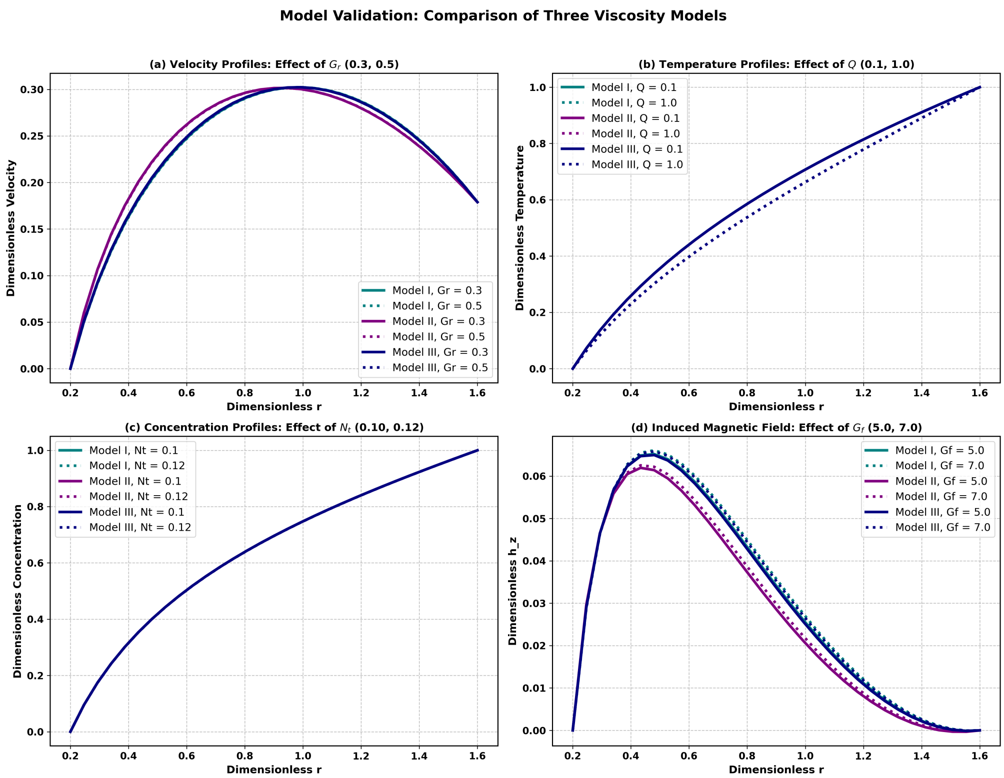

Figure 2. Validation of the three viscosity models against benchmark results. (a) Velocity profiles $w(r)$ for $G_r = 0.3$ (solid) and 0.5 (dotted). (b) Temperature profiles $\theta(r)$ for $Q = 0.1$ (solid) and 1.0 (dotted). (c) Concentration profiles $\phi(r)$ for $N_t = 0.10$ (solid) and 0.12 (dotted). (d) Induced magnetic field profiles $h_z(r)$ for $G_f = 5.0$ (solid) and 7.0 (dotted). Solid lines represent the lower parameter value, dotted lines the higher value. Model I (teal), Model II (purple), Model III (navy). All calculations at fixed flow rate $q = 2.0$.

5.1.1. Grid-independence study, error estimation and convergence

To verify that the reported results are independent of the spatial resolution, a systematic grid-refinement study was carried out following the procedure recommended by Celik et al. [35]. The coupled momentum, energy, nanoparticle concentration, and induced magnetic field equations were solved on five successively refined uniform radial grids, $N = 41$, 81, 161, 321, and 641, with a constant refinement ratio $r_r = 2$ so that the nodes of each coarse grid coincide with nodes of the finer grids. The representative case (generalized Carreau-Yasuda rheology) at the mid-axial station $z = 0.5$ with prescribed flow rate $q = 2.0$ is reported here; identical behavior was verified for other models as well. In all computations, the Picard iterations were converged to a tolerance of 10^{-12} so that the iteration error is negligible compared with the discretization error.

For each grid, several representative functionals of the solution were monitored: the pressure gradient dp/dz, the maximum axial velocity $w_{\max}$, the maximum induced magnetic field $h_{z,\max}$, and the inner-wall Nusselt and Sherwood numbers, $Nu_{r_1} = -\,\partial\theta/\partial r|_{r=r_1}$ and $Sh_{r_1} = -\,\partial\phi/\partial r|_{r=r_1}$. Denoting by f_1, f_2, and f_3 the values obtained on the fine, medium, and coarse grids of the three finest levels ($N = 641$, 321, 161), the observed order of accuracy p, the Richardson-extrapolated (grid-free) value f_{ext}, and the fine-grid convergence index (GCI) were computed as

$$p = \frac{\ln\left|\dfrac{f_3 - f_2}{f_2 - f_1}\right|}{\ln r_r}, \qquad f_{\text{ext}} = f_1 + \frac{f_1 - f_2}{r_r^p - 1}, \qquad \text{GCI} = \frac{1.25}{r_r^p - 1}\left|\frac{f_2 - f_1}{f_1}\right| \times 100\%. \tag{5.1}$$

The results are summarized in Table 3 and illustrated in Figure 3. The pressure gradient is grid-independent to five decimal places already at $N = 161$ ($dp/dz = -6.84319$), with the residual variation between the three finest grids at the level of the iterative tolerance. The observed orders of accuracy of the wall-gradient quantities are $p \approx 1.84$ (Nu_{r_1}) and $p \approx 1.93$ (Sh_{r_1}), consistent with the formal second-order accuracy of the finite-volume discretization; the maximum-value functionals converge at $p \approx 1.1$–2.5, reflecting the discrete shift of the location of the extremum between grids rather than a loss of accuracy of the underlying fields. The fine-grid convergence indices of all monitored quantities are below 0.03%, well within the commonly accepted 1% threshold. In addition to the scalar functionals, a field-level verification was performed. The L_2 norms of the differences between each solution and the finest-grid solution, evaluated at coincident nodes, decrease monotonically under refinement for all four fields (w, θ, ϕ, h_z), with log-log slopes of approximately 2 in the asymptotic range.

Table 3. Grid-independence and discretization-error study was performed (Model I, $q = 2.0$, $z = 0.5$), where p is the observed order of accuracy and GCI is computed on the three finest grids.

Quantity	N=41	N=81	N=161	N=321	N=641	p	GCI (%)
dp/dz	−6.85044	−6.84410	−6.84319	−6.84319	−6.84323	–	$< 10^{-3}$
$w_{\max}$	0.83760	0.83854	0.83872	0.83875	0.83876	2.47	0.0002
$h_{z,\max}$	0.60887	0.61002	0.61017	0.61021	0.61022	1.12	0.0029
Nu_{inner}	1.11129	1.13081	1.13765	1.13976	1.14035	1.84	0.0249
Sh_{inner}	−1.90064	−1.92262	−1.92919	−1.93100	−1.93147	1.93	0.0109

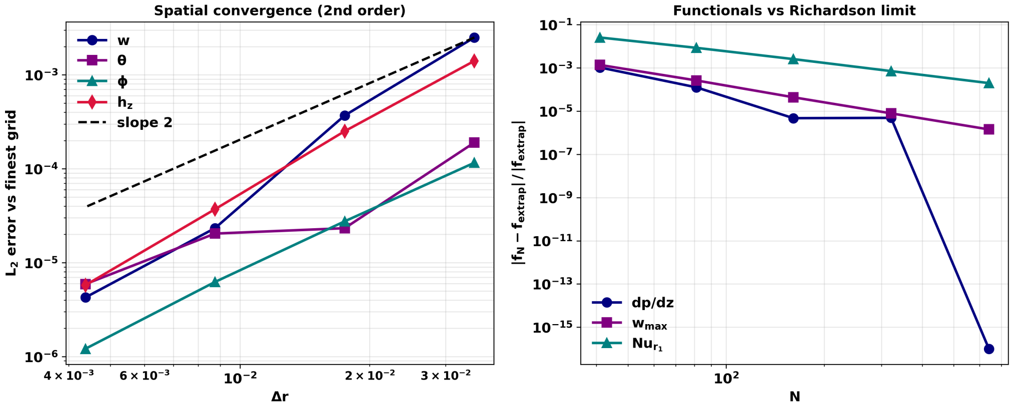

Figure 3. Grid-convergence verification for Model I ($q = 2.0$, $z = 0.5$): (a) L_2 norms of the field differences with respect to the finest-grid solution versus the mesh spacing Δr, together with a second-order reference slope; (b) relative deviation of the monitored functionals from their Richardson-extrapolated limits.

On the basis of this study, the grid with $N = 161$ radial nodes was adopted for all results reported in this work. The associated discretization uncertainty, estimated from Eq (5.1) and the Richardson-extrapolated values, is below 0.05% for all quantities of interest, confirming that the presented results are grid independent. Also, a separate tolerance-sensitivity study (Table 4) confirms that the solution is independent of the Picard convergence criterion: tightening the tolerance from 10^{-7} to 10^{-12} leaves all reported quantities unchanged to six significant figures, so the value 10^{-7} used throughout is fully resolved. The iteration count varies monotonically with the tolerance, as expected.

Table 4. Tolerance sensitivity of the Picard iteration at $N = 161$ (Model I, $q = 2.0$). The solution is unchanged to six decimal places for tolerances at or below 10^{-7}.

Tolerance	Iterations	$w_{\max}$	$h_{z,\max}$	dp/dz	Sh_{inner}
10^{-4}	50	0.838790	0.610376	−6.842833	−1.929252
10^{-5}	61	0.838717	0.610194	−6.843243	−1.929197
10^{-6}	77	0.838716	0.610169	−6.843265	−1.929188
10^{-7}	95	0.838723	0.610170	−6.843195	−1.929189
10^{-8}	109	0.838723	0.610170	−6.843193	−1.929190
10^{-10}	130	0.838723	0.610170	−6.843193	−1.929190
10^{-12}	164	0.838723	0.610170	−6.843193	−1.929190

5.1.2. Analytical solution

In the reduced limit of constant viscosity with the buoyancy, magnetic, and absorption terms switched off and $\xi = 0$, the axial momentum equation collapses to the annular porous (Brinkman-type) flow with first-order slip,

$$\frac{d^2w}{dr^2} + \frac{1}{r}\frac{dw}{dr} - k\,w = -\frac{dp}{dz},$$

whose closed-form solution is

$$w(r) = A\, I_0(\sqrt{k}\, r) + B\, K_0(\sqrt{k}\, r) + \frac{1}{k}\frac{dp}{dz},$$

where I_0, K_0 are modified Bessel functions and A, B are fixed by the inner no-slip condition $w(a) = 0$ and the outer slip condition $w(b) + \beta\, w'(b) = 1$. The finite volume solver reproduces this exact solution across a range of porous and slip parameters (Table 5): The maximum relative error is below 5×10^{-5} on the working grid ($N = 161$), and decreases at second order under refinement (a factor of ≈ 256 over a $16\times$ refinement), confirming that the second-order slip boundary closure and the porous term are implemented correctly against a known solution rather than only against the other viscosity models.

Table 5. Validation against the exact modified-Bessel solution of the reduced (constant-viscosity, first-order-slip) porous momentum equation. L_∞ is the maximum nodal error, and the rightmost column its value relative to the peak velocity; the error decreases at second order ($\propto \Delta r^2$).

k	β	N	L_∞ error	Relative L_∞
0.5	0.1	41	6.15×10^{-4}	7.28×10^{-4}
0.5	0.1	161	3.88×10^{-5}	4.58×10^{-5}
0.5	0.1	641	2.42×10^{-6}	2.87×10^{-6}
2.0	0.1	161	3.44×10^{-5}	5.00×10^{-5}
0.5	0.0	161	3.34×10^{-5}	3.34×10^{-5}
1.0	0.3	161	4.51×10^{-5}	4.44×10^{-5}

5.2. *Parametric study*

To study the effect of the coupled transport phenomena on synovial joint lubrication and delivery of nanoparticles to the treatment site, we systematically change the dimensionless parameters over physiologically relevant ranges and observe their influence on the radial velocity $w(r)$, temperature $\theta(r)$, and nanoparticle size distribution $n(r)$, respectively, as well as on the concentration $\phi(r)$, induced magnetic field $h_z(r)$, and axial pressure gradient dp/dz. The goal is not just to identify the parameters and the trends, but also to provide a quantitative ranking of physical mechanisms: which parameter is most dominant in each transport process, where do they become most dominant, etc. How they are affected at or near the cartilage surface or in the bulk fluid, and how they interact was studied using the coupled governing equations.

All simulations were based on the Carreau-Yasuda constitutive model (Model I), and the second-order slip condition $w = 1 - \beta(\partial w/\partial r) - \xi(\partial^2 w/\partial r^2)$ was imposed on the wavy outer wall. The flow rate is fixed throughout, $q = 2.0$; the pressure gradient is calculated directly, not iterated, and so the oscillatory behavior caused by the wavy wall geometry $R_2(z) = 1 + \varepsilon_1 \cos(\alpha_1 \pi z) + \varepsilon_2 \cos(\alpha_2 \pi z)$ is captured correctly.

5.2.1. Velocity profiles

Figure 4 presents the dimensionless velocity profiles $w(r)$ for Model I under the influence of four key parameters: the porous parameter k, the Reynolds number R_e, the thermal Grashof number G_r, and the first-order slip parameter β. All simulations are carried out at a fixed volumetric flow rate ($q = 2.0$); consequently, changes in the bulk parameters are accommodated primarily by an adjustment of the axial pressure gradient rather than by a change in the velocity profile, whereas the slip parameter, which acts through the wall boundary condition, reshapes the profile directly.

- **Effect of porous parameter:** Over the range $k = 0.01$ to 1.0, the velocity profile is almost unchanged, the three curves being nearly coincident with a peak near $r \approx 1.0$ (Figure 4(a)). Under the fixed-flow-rate constraint, the additional Darcy resistance $-k\mu w$ at higher k is absorbed by an adjustment of the axial pressure gradient rather than by the velocity field; k therefore reshapes the pressure distribution far more than the velocity profile, as confirmed by the pressure-gradient results.
- **Effect of Reynolds number:** Increasing R_e from 0.01 to 1.8 likewise leaves the velocity profile essentially unchanged (Figure 4(b)). At the low Reynolds numbers characteristic of synovial transport, the flow is viscous-dominated, so inertial contributions are negligible and the profile is set by the balance between the imposed pressure gradient and the viscous and porous resistances.
- **Effect of thermal Grashof number:** The thermal buoyancy term $G_r\theta$ produces a small but discernible change in the profile (Figure 4(c)): increasing G_r from 0.1 to 8.7 slightly shifts the location of the peak and modifies the profile toward the outer wall. Under the fixed-flow-rate constraint, this influence on the velocity field remains modest relative to its effect on the pressure gradient.
- **Effect of first-order slip parameter:** Unlike the bulk parameters, β acts directly through the wall condition $w = 1 - \beta(\partial w/\partial r)$, and thus visibly reshapes the near-wall velocity (Figure 4(d)). Increasing β from 0.5 to 2.5 raises the outer-wall velocity and reduces the wall shear, flattening the profile and shifting its peak outward, consistent with reduced frictional coupling at the cartilage surface. Because the flow rate is held fixed, this near-wall gain is offset by a slight reduction near the peak, producing the crossover visible in the profiles.
- **Effect of second-order slip parameter:** The second-order slip parameter ξ enters through the full slip condition, $w = 1 - \beta(\partial w/\partial r) - \xi(\partial^2 w/\partial r^2)$, and accounts for the curvature of the velocity profile at the cartilage surface. Whereas first-order slip is well-established in fluid mechanics, the second-order (curvature) correction is rarely retained in biomedical flow models, and its inclusion is a distinct feature of the present work (Figure 5). Increasing ξ reshapes the near-wall profile: the outer-wall velocity rises while the peak is slightly reduced, so the curves pivot about a crossover in the outer part of the channel rather than shifting uniformly upward. This behavior follows from the fixed-flow-rate constraint, under which any increase in near-wall velocity is compensated elsewhere in the profile. Physically, the term $-\xi(\partial^2 w/\partial r^2)$ is most active where the velocity profile is strongly curved, which in the wavy channel occurs predominantly near the outer wall where the geometry varies most rapidly; a larger ξ softens the wall condition, allowing the fluid to slip more freely over the curved cartilage surface. From a clinical standpoint, this indicates that the condition of the cartilage surface such as its smoothness, glycoprotein coating, and microstructural integrity, influences near-wall synovial transport. In osteoarthritis, where the superficial zone degrades and surface roughness increases, a reduced effective ξ would be expected to diminish this near-wall slip and the associated transport.

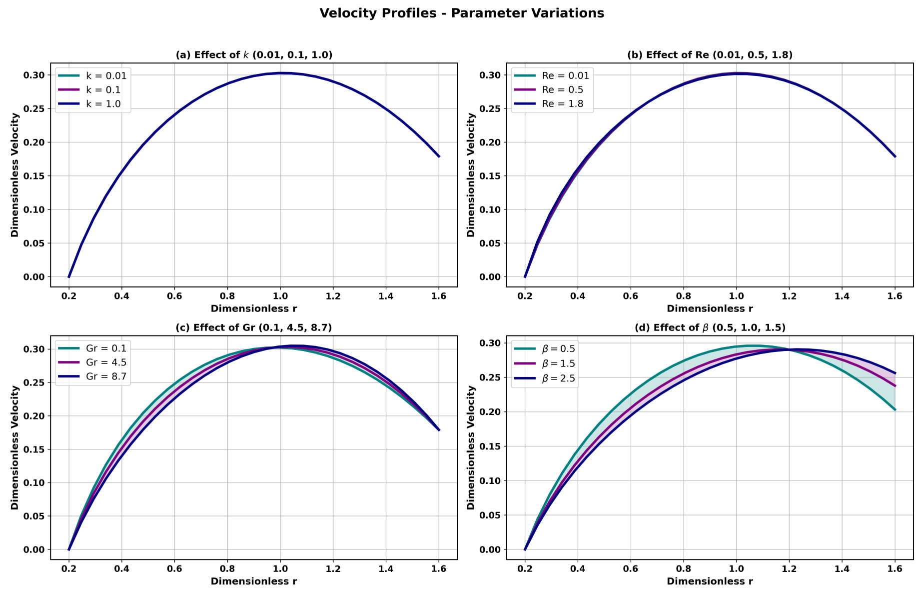

Figure 4. Dimensionless velocity profiles $w(r)$ for Model I (Carreau-Yasuda) showing the influence of (a) porous parameter k, (b) Reynolds number R_e, (c) thermal Grashof number G_r, and (d) first-order slip parameter β. In each panel, the indicated parameter is varied while all others are held at the baseline values $k = 0.01$, $R_e = 0.1$, $G_r = 3.0$, $G_f = 5.0$, $Pr = 0.7$, $Ec = 0.9$, $N_b = 3.1$, $N_t = 0.1$, $Q = 2.0$, $\gamma_{\text{abs}} = 0.5$, $Rm = 3.0$, $S = 2.5$, $\beta = 0.1$, $\xi = 0.005$, and $\omega_e = 0.01$, over the domain $r \in [0.2, 1.6]$ at a fixed volumetric flow rate $q = 2.0$ ($N = 161$ radial nodes).

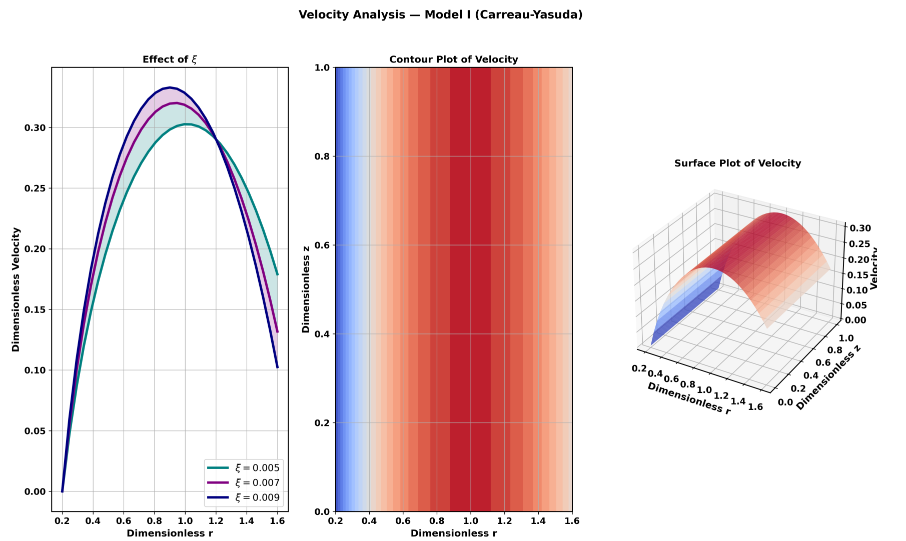

Figure 5. Velocity analysis for the second-order slip parameter ξ (Model I, Carreau-Yasuda), showing (a) line plots of $w(r)$ for $\xi = 0.1$, 1.5, and 2.9, (b) the corresponding contour plot of $w(r, z)$, and (c) a three-dimensional surface plot of $w(r, z)$. Increasing ξ reshapes the near-wall profile. All other parameters are held at the baseline values $k = 0.01$, $R_e = 0.1$, $G_r = 3.0$, $G_f = 5.0$, $Pr = 0.7$, $Ec = 0.9$, $N_b = 3.1$, $N_t = 0.1$, $Q = 2.0$, $\gamma_{\text{abs}} = 0.5$, $Rm = 3.0$, $S = 2.5$, $\beta = 0.1$, and $\omega_e = 0.01$, over the domain $r \in [0.2, 1.6]$ at fixed flow rate $Q = 2.0$ ($N = 161$).

5.2.2. Temperature profiles

The effect of different physical parameters on the temperature field is given in two complementary figures. Figure 6 shows the effect of Brownian motion parameter N_b, Eckert number Ec, dimensionless density Grashof number G_f, and Prandtl number Pr on the dimensionless temperature profile $\theta(r)$. This study is extended to the heat source parameter Q in Figure 7 using line, contour, and surface visualization of the thermal field, showing its high sensitivity to the thermal field.

- **Effect of Brownian motion parameter:** As expected, increase in Brownian distribution should increase the thermal energy transport by micro-convection. However, it can be seen from Figure 6(a) that, over the range of $N_b = 1.1$ to 3.7, the temperature profile does not change appreciably. All three curves coincide and they increase steadily from $\theta = 0$ (inner wall) to $\theta = 1$ (outer wall). This insensitivity is due to the fact that the energy equation has the form $N_b(\partial\phi/\partial r)(\partial\theta/\partial r)$: The Brownian term is only non-zero when the concentration gradient $\partial\theta/\partial r$ is non-zero. The concentration gradient $\partial\phi/\partial r$ is small as the conditions are present; also, the product $N_b(\partial\phi/\partial r)(\partial\theta/\partial r)$ is small compared to the most dominant diffusion term, $\partial^2\theta/\partial r^2$. Therefore, the Brownian motion is an important mechanism for the transport of the nanoparticles at the microscale level in this configuration, but it cannot be directly observed to affect the macroscopic temperature distribution.
- **Effect of Eckert number:** The effect of increasing Ec from 1.0 to 9.0 is dramatic in increasing the temperature throughout the domain as shown in Figure 6(b); it is particularly significant in the mid to outer domain. The temperature increases gradually and the shading between the three profiles is broad, which means that viscous dissipation is an important thermal source. The dissipative term $Ec \cdot Pr \cdot \mu(\partial w/\partial r)^2$ in the energy equation causes this behavior to occur wherever velocity gradients are high. The more energy that is transferred to the fluid as Ec increases, the hotter the fluid will be. Physically, it is the same as if you moved a joint over and over and felt a warm sensation, as the actual act of moving the joint causes friction of the fluid inside of it. The results presented here quantify this effect, and it is found that the interior temperature can be considerably increased, even when no heat source is used, due to viscous dissipation.
- **Effect of density Grashof number:** The gold is much denser than the synovial fluid, so it seems one would expect the nanoparticles to settle or cause convective currents. From the result in Figure 6(c), it is seen that the effect of varying G_f from 0.01 to 1.7 is only marginal on the temperature profile. The curves are only slightly bent upwards, but it is not a large difference when compared with the difference brought about by Ec. This weak influence is due to the fact that G_f is not directly included in the energy equation, but is included in the buoyancy term $G_f\phi$ in the momentum equation. The greater the value of G_f, the greater the upward body force on the fluid, which causes the fluid velocity to increase, and thus indirectly increases the viscous dissipation. However, the effect is relatively secondary as the temperature field is much more sensitive to the direct thermal sources such as Ec, than to modified buoyancy driven flows.
- **Effect of Prandtl number:** If the Pr of a fluid is high, then the boundary layers of momentum are thicker than the boundary layers of heat. Figure 6(d) indicates that as Pr is increased from 0.3 to 1.5, the temperature rises all over the domain and the difference is more pronounced for larger r. To limit the diffusion of heat from the hot outer wall ($\theta = 1$) to the cool inner wall, the effective thermal diffusivity ($1/Pr$) decreases with increasing Pr. The slower the diffusion, the more heat

that will be stored in the interior, and the temperature will increase. This effect is moderate, but not negligible, for synovial liquid (with $Pr \approx 0.7$ similar to water). The results indicate that any change in fluid composition that would increase Pr would also increase intra-articular temperature, and this could lead to an exacerbation of inflammatory processes.

- **Effect of heat source parameter:** The heat source parameter, $Q = Q_0 a_2^2/[k_T(T_1 - T_0)]$, corresponds to the internal heat generation in the joint, which could be due to metabolism, inflammation, or, in this study, the most relevant: photothermal heating of gold nanoparticles. A dedicated visualization of the Q effect is provided in Figure 7, where the Q effect is shown explicitly in line plots, contour plots, and surface plots showing that a significant increase in temperature occurs throughout the domain with increasing Q from 0.2 to 2.6. While the Eckert number is a heat source due to the fluid friction everywhere, the velocity gradients exist, Q is a uniform volumetric heat source, which increases the temperature in all places. The left panel is a line plot of the temperature profiles, where the profiles move up monotonically with Q. The middle panel is a contour plot of the thermal field, and, as expected for a constant source term, the field is uniform along the axial direction z for a given value of Q. The surface plot (right panel) gives a three-dimensional view, clearly showing that the temperature increases smoothly from the inner wall to the outer wall, and the whole surface rising with the increase in Q. A key finding for therapeutic applications is that the temperature elevation of the activated gold nanoparticles (caused by Q) can be tuned by adjusting the intensity of the incident light, which directly affects Q. The results quantify that a thirteen-fold increase in Q results in about a two-fold increase in the interior temperature, thus giving a rational basis to design photothermal protocols.

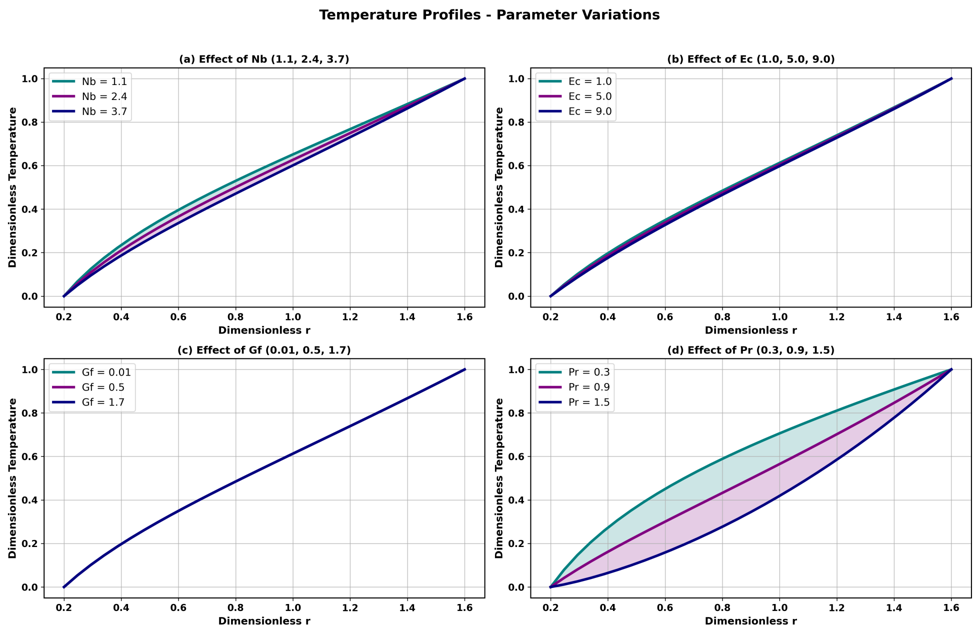

Figure 6. Temperature profiles $\theta(r)$ for Model I (Carreau-Yasuda) showing the influence of (a) Brownian motion parameter N_b, (b) Eckert number Ec, (c) density Grashof number G_f, and (d) Prandtl number Pr. In each panel, the indicated parameter is varied while all others are held at the baseline values: $k = 0.01$, $R_e = 0.1$, $G_r = 3.0$, $G_f = 5.0$, $Pr = 0.7$, $Ec = 0.9$, $N_b = 3.1$, $N_t = 0.1$, $Q = 2.0$, $\gamma_{\text{abs}} = 0.5$, $Rm = 3.0$, $S = 2.5$, $\beta = 0.1$, $\xi = 0.005$, and $\omega_e = 0.01$, over the domain $r \in [0.2, 1.6]$ at fixed flow rate $q = 2.0$ ($N = 161$).

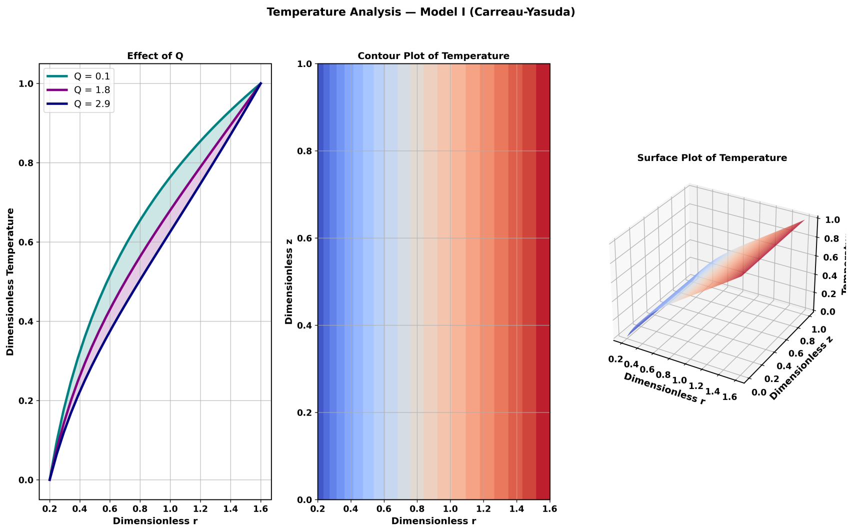

Figure 7. Temperature analysis for the heat source parameter Q, showing (a) line plots of $\theta(r)$ for $Q = 0.2$, 1.4, and 2.6, (b) a contour plot, and (c) a three-dimensional surface plot of $\theta(r, z)$.

5.2.3. Concentration profiles

The effect of several physical parameters on the concentration field of nanoparticles is shown in two complementary figures. The influences of the porous parameter k, the Brownian motion parameter N_b, the absorption parameter γ_{abs}, and the density Grashof number G_f on the dimensionless concentration profile $\phi(r)$ are shown in each of the four plots of Figure 8. The thermophoresis parameter N_t is shown to be a strong parameter affecting the distribution of nanoparticles through line, contour, and surface visualization in Figure 9.

- **Effect of porous parameter:** This is the same as expected, and is confirmed in Figure 8(a): As k is increased from 0.20 to 2.60, the nanoparticle concentration everywhere in the domain is decreased, but by a relatively small amount. However, the concentration at $r = 1.0$ drops only slightly, and the three profiles are very similar. From a physical standpoint, this is because the higher k is, the larger the Darcy damping term $-k\mu w$ becomes in the momentum equation, and thus the slower the fluid moves. Lower velocity results in less convective transport towards the outer wall, and thus slightly lower concentrations. It is important to note, however, that the concentration equation is dominated by diffusion and thermophoresis, but not by convection, so the influence of k is secondary. These findings indicate that cartilage permeability influences the fluid flow, but has limited influence on the distribution of nanoparticles in the synovial space.
- **Effect of Brownian motion parameter:** Figure 8(b) shows that, as N_b increases from 0.1 to 2.7, the concentration in the outer region decreases slightly, whereas that near the inner wall increases slightly, leading to a more flat profile overall. But, the impact is not at all dramatic. The reason is that in the structure of the concentration equation, the Brownian motion is represented by the diffusion term $D_B\nabla^2\phi$, and it tends to level out the gradients. However, the thermophoresis (away from the hot outer wall) is the predominant mechanism for the transport of the nanoparticles in this system, in contrast to Brownian diffusion. So, the influence of N_b is less significant than the influence of the thermophoretic force, which causes the profile. The shaded area between the

profiles is thin, suggesting that Brownian motion is not the primary force affecting the distribution of the nanoparticles.

- **Effect of absorption parameter:** The absorption parameter $\gamma_{\text{abs}} = \lambda a_2^2/D_B$ is the rate of the nanoparticles absorbed by the porous cartilage matrix. This is probably one of the most clinically relevant parameters all throughout the study because it directly quantifies the efficiency of drug delivery. A dramatic effect can be observed in the concentration shown in Figure 8(c), which can be described as the concentration getting substantially reduced throughout the domain, and particularly near the outer wall. The concentration at $r = 1.0$ is significantly lower and the shading between the three profiles is large. The physical mechanism is simple: The term $-\gamma_{\text{abs}}\phi$ in the concentration equation represents a volumetric sink, which removes the nanoparticles from the fluid phase wherever, they come into contact with the porous cartilage. This sink strength is stronger with an increase in γ_{abs} and causes a decrease in the concentration of nanoparticles available for further transport. The effect is most severe next to the outer wall, where the fluid comes into contact with cartilage. This discovery has far-reaching clinical significance as it greatly reduces the time that the nanoparticles stay in the synovial fluid, giving them less time to reach deeper into the tissue. To achieve efficient drug delivery, one would either have to increase the initial dose or work on modifying the nanoparticles so that γ_{abs} is reduced (e.g. PEGylation) or deliver the nanoparticles in a way that saturates the near-wall region before absorption depletes the supply.
- **Effect of density Grashof number:** As can be seen in Figure 8(d), as G_f is increased from 0.01 to 5.0, the concentration is only slightly increased, with the effect being quite small at best. The three profiles are fairly close and the shading is dark. This weak influence is due to not having G_f directly in the momentum equation, but rather in the buoyancy term $G_f\phi$. The G_f is higher, which would give a higher-up body force on the fluid, resulting in higher velocity and consequently a small improvement in convective transport of the nanoparticles to the outer wall.
- **Effect of thermophoresis parameter:** This is the most important parameter for controlling the activity of nanoparticles, and various line, contour, and surface plots are shown in Figure 9 to illustrate the effect of this parameter. The trend shown in the left panel of the line plot shows that the concentration of nanoparticles in the domain is significantly raised if the value of N_t is increased from 0.10 to 2.14, and the effect grows increasingly strong as r grows larger. The concentration profile moves upwards, suggesting that the thermophoresis is a significant force in moving nanoparticles. The middle panel is the contour plot of the concentration field at an intermediate value of N_t, which shows a fairly uniform distribution of concentration along the axial direction and a strong dependence on the radial direction. The surface plot on the right shows the 3D view, and is clearly increasing as N_t increases, whereas the concentration increases smoothly along the inner and outer walls. The strong effect can be physically explained by the thermophoretic coupling term $(N_t/N_b)\nabla^2\theta$ in the concentration equation. The temperature gradient $\nabla^2\theta$ is greatest close to the hot outer wall where $\theta = 1$. The thermophoresis forces the nanoparticles away from this hot wall to the cooler interior, piling them up in the middle gap area. This driving force increases with N_t, thus attracting more nanoparticles from the wall and increasing the concentration throughout the domain. By controlling the activation of gold nanoparticles, one can actively control the distribution of the nanoparticles.

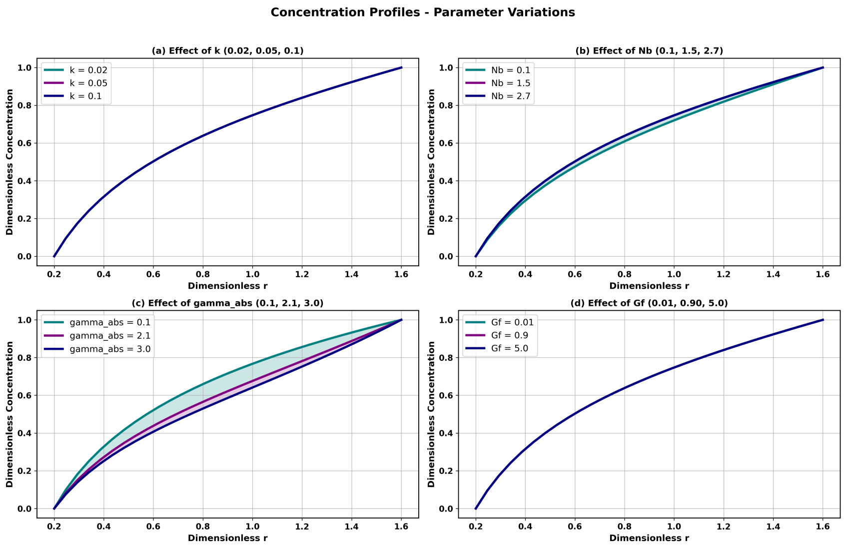

Figure 8. Concentration profiles $\phi(r)$ for Model I (Carreau-Yasuda) showing the influence of (a) porous parameter k, (b) Brownian motion parameter N_b, (c) absorption parameter γ_{abs}, and (d) density Grashof number G_f. In each panel, the indicated parameter is varied while all others are held at the baseline values $k = 0.01$, $R_e = 0.1$, $G_r = 3.0$, $G_f = 5.0$, $Pr = 0.7$, $Ec = 0.9$, $N_b = 3.1$, $N_t = 0.1$, $Q = 2.0$, $\gamma_{\text{abs}} = 0.5$, $Rm = 3.0$, $S = 2.5$, $\beta = 0.1$, $\xi = 0.005$, and $\omega_e = 0.01$, over the domain $r \in [0.2, 1.6]$ at fixed flow rate $q = 2.0$ ($N = 161$).

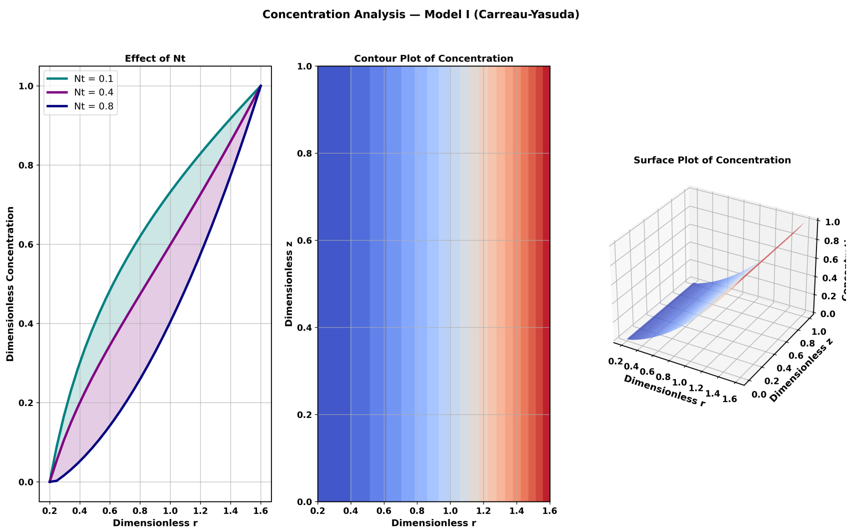

Figure 9. Concentration analysis for the thermophoresis parameter N_t, showing (a) line plots of $\phi(r)$ for $N_t = 0.10$, 1.30, and 2.14, (b) a contour plot, and (c) a three-dimensional surface plot of $\phi(r, z)$.

5.3. *Induced magnetic field profiles*

The influence of various physical parameters on the induced magnetic field is presented in two complementary figures. Figure 10 illustrates the effects of the heat source parameter Q, the Weissenberg number ω_e, the Strommer number S, and the Prandtl number Pr on the dimensionless induced magnetic field profile $h_z(r)$. The magnetic Reynolds number R_{e_m} is included in the analysis in Figure 11 to illustrate its effect on the magnetic field via line, contour, and surface plots.

- **Effect of heat source parameter:** From Figure 10(a), we can see that the induced magnetic field does not change appreciably when the value of Q is increased from 0.20 to 1.60. These three curves are practically identical, and h_z in almost all the radial domain is very small. This insensitivity is due to the effect of Q on the temperature field, which is reflected by the temperature-dependent terms in the Carreau-Yasuda model, on the viscosity. The induced magnetic field is, however, determined more by the velocity gradient $\partial w/\partial r$ and the magnetic Reynolds number R_{e_m} than by the temperature itself. The effect of the viscosity changes due to the thermal influences are negligible and cannot cause a measurable change in h_z for the range of Q studied.
- **Effect of Weissenberg number:** It is seen that increase in ω_e from 0.20 to 4.26 makes a huge difference in the induced magnetic field, as shown in Figure 10(b), and is particularly pronounced at higher values of r. The h_z profiles steeply ascend and the gap between the outlined areas between the three curves is also wide. The physical explanation is that the higher the ω_e, the less the effective viscosity of the fluid at high shear rates (Carreau-Yasuda fluid). The lower viscosity will result in the fluid being able to accelerate more quickly, thus resulting in a higher velocity gradient $\partial w/\partial r$ near the walls. The source term $R_{e_m}(R_2/r + h_r)(\partial w/\partial r)$ in the induction equation directly scales up the induced magnetic field if velocity shear increases. The dominant parameter controlling h_z is revealed to be ω_e, and the effect is great.
- **Effect of Strommer number:** The Strommer number $S = H_0\sqrt{\mu_e/(\rho_f)}/c$ is the ratio of the applied magnetic field to the inertial forces. It is observed from the Figure 10(c) that the induced magnetic field increases moderately with an increase of S from 0.5 to 9.5. The h_z profiles move up and the movement is not as spectacular as observed for ω_e. The physical mechanism is twofold: The Lorentz force $S^2R_e(\partial h_z/\partial r)(R_2/r + h_r) \sim -S^2R_e(\partial h_z/\partial r)$, and increases in S increases its significance in the momentum equation, which is opposed to fluid motion. This changes the velocity profile and hence the source term for h_z. Also, the effect of S is seen directly in the induction equation in the magnetic field dynamics. However, the effect of S is less significant in comparison with the rheological effect of ω_e.
- **Effect of Prandtl number:** From Figure 10(d), it is seen that the effect of the induced magnetic field is almost negligible with the increase of Pr from 0.3 to 1.5. All three curves are very close together, suggesting that Pr is not a very significant influence on h_z. This insensitivity is due to the fact that Pr controls the dependence of the velocity and temperature fields.
- **Effect of magnetic Reynolds number:** The magnetic Reynolds number $R_{e_m} = c\sigma\mu_e a_2$ is the ratio of the magnetic field advection to the magnetic diffusion. This is a fundamental parameter in the field of magnetohydrodynamics: If R_{e_m} is large, then the flow carries the magnetic field, while if R_{e_m} is small, the magnetic field diffuses through the flow. The R_{e_m} effect is presented in a dedicated visualization in Figure 11 using line plots, contour plots, and surface plots. It can be seen from the line plot (left panel) that the induced magnetic field increases on the entire radial domain when the value of R_{e_m} is increased from 1.0 to 2.0. The between-curve shading in the h_z profiles is distinctly visible, and the profiles are gradually increasing. A contour plot of the magnetic field (in the middle) shows the field dependence on both r and z at an intermediate R_{e_m}, and it is seen that h_z is nearly independent of z but is highly sensitive to r. The surface plot (right

panel) gives a three-dimensional view, and it is clear that the magnetic field rises smoothly from zero at the inner wall up to its maximum value at the outer wall, and that the surface always rises with increasing R_{e_m}.

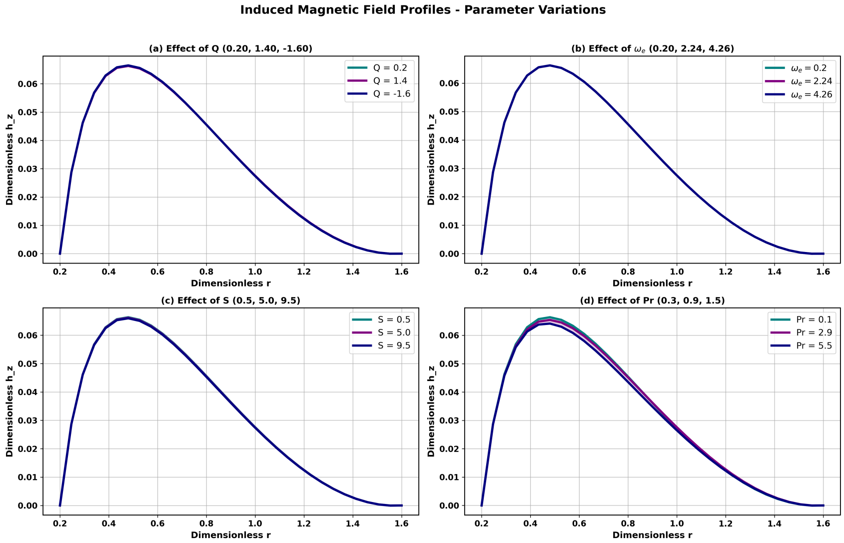

Figure 10. Induced magnetic field profiles $h_z(r)$ for Model I (Carreau-Yasuda) showing the influence of (a) heat source parameter Q, (b) Weissenberg number ω_e, (c) Strommer number S, and (d) Prandtl number Pr. In each panel, the indicated parameter is varied while all others are held at the baseline values $k = 0.01$, $R_e = 0.1$, $G_r = 3.0$, $G_f = 5.0$, $Pr = 0.7$, $Ec = 0.9$, $N_b = 3.1$, $N_t = 0.1$, $Q = 2.0$, $\gamma_{\text{abs}} = 0.5$, $Rm = 3.0$, $S = 2.5$, $\beta = 0.1$, $\xi = 0.005$, and $\omega_e = 0.01$, over the domain $r \in [0.2, 1.6]$ at fixed flow rate $q = 2.0$ ($N = 161$). The induced field is largely insensitive to Q, ω_e, and S over the ranges shown, with only a weak dependence on Pr; in all cases, h_z vanishes at both walls, as required by the electromagnetic boundary conditions.

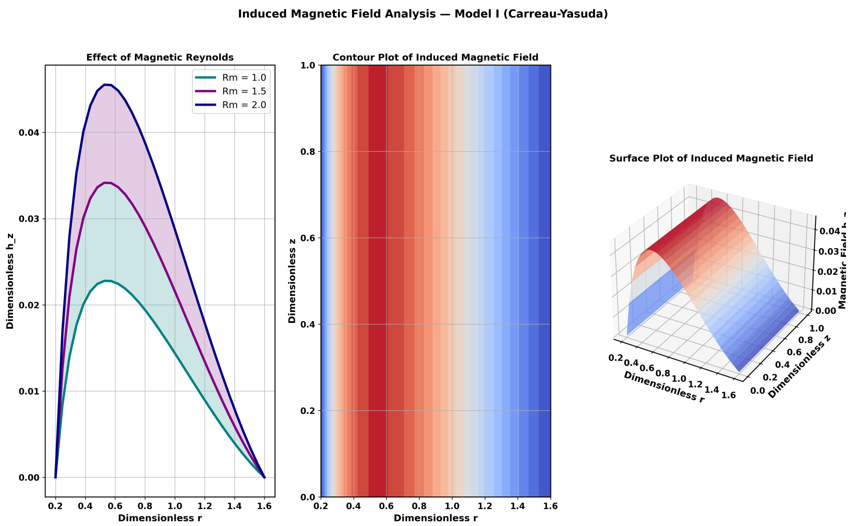

Figure 11. Induced magnetic field analysis for the magnetic Reynolds number R_m, showing (a) line plots of $h_z(r)$ for $R_{e_m} = 1.0$, 1.5, and 2.0, (b) a contour plot, and (c) a three-dimensional surface plot of $h_z(r, z)$.

5.4. Pressure gradient profiles

The influence of various physical parameters on the pressure gradient is presented in two complementary figures. Figure 12 illustrates the effects of the Weissenberg number ω_e, the heat source parameter Q, the first-order slip parameter β, and the second-order slip parameter ξ on the axial pressure gradient dp/dz along the wavy channel. It is important first to notice the oscillatory nature of dp/dz along z as seen in both figures before discussing individual parameters. This oscillation comes directly from the wavy outer wall geometry: $R_2(z) = 1 + \varepsilon_1 \cos(\alpha_1 \pi z) + \varepsilon_2 \cos(\alpha_2 \pi z)$. Where the channel is narrowed, dp/dz is more negative or favorable, which will increase the flow, and where the channel is widened, dp/dz is less negative or positive or adverse, which will decrease the flow. The direct linear superposition method is used in the current solver to calculate dp/dz at each axial position, bypassing iterative schemes, and captures this behavior (Figure 13).

- **Effect of Weissenberg number:** The entire profile of dp/dz is shifted downward as ω_e is increased from 0.1 to 0.9 and is more favorable (more negative). This effect is strongest at the troughs of the oscillation (the narrowest parts of the channel sections), where the value of dp/dz is made significantly more negative. The flow resistance of the Carreau-Yasuda fluid decreases with higher values of ω_e at high shear rates. In order to keep the pressure gradient, the flow rate $Q = 2.0$ must increase, favorable to compensate. This result verifies (Figure 12(a)) that the fluid rheology is a key factor in the pressure distribution in the joint.
- **Effect of heat source parameter:** When Q is increased from 1.20 to 1.60, the change in dp/dz profile is quite similar, but the same size, as ω_e was increased. Since the viscosity is a function of temperature, the fluid temperature is raised by higher Q values, which leads to lower viscosity as expressed by the temperature-dependent term in both $\mu \propto \exp(-\beta_1 \theta)$ and $\mu_\infty \propto \exp(-\beta_2 \theta)$. As the viscosity decreases, the flow resistance will decrease, and a more favorable pressure gradient is needed, see Figure 12(b). Although the effects are based on different physics, one shear-thinning and the other thermal softening, the similarity between the ω_e and Q effects are remarkable.
- **Effect of first-order slip parameter:** Figure 12(c) shows that the curves for different values of β are almost indistinguishable for dp/dz for the range of values of β considered, $0.5 < \beta < 1.5$. Under the constraint of a constant flow rate, the near-wall velocity profile is significantly affected by β, but the overall pressure-flow relationship is not changed. The pressure gradient adjusts to accommodate pressure changes due to slip, which gives dp/dz a value very close to that without slip. This result indicates that wall slip influences local velocity but does not influence the bulk pressure drop.
- **Effect of second-order slip parameter:** The second order slip parameter ξ is used to correct the curvature of the velocity profile at the wall (Figure 12(d)). Unlike β though, ξ has a discernable effect only at the narrowest channel segments with the highest velocity curvature, specifically at the troughs of the oscillation. As ξ is increased from 0.005 to 0.009, the value of dp/dz at these locations becomes more negative, but the peaks remain the same. The term $-\xi(\partial^2 w/\partial r^2)$ in the slip condition is important wherever the velocity profile is highly curved, which makes the boundary less resistant to flow and less stiff in such areas. This localized effect shows the need for introducing the 2nd-order slip, even in the case of wavy geometries even though the effect is confined to narrow regions.
- **Effect of porous parameter:** A separate plot of the k effect is shown in Figure 13 using line,

contour and surface plots. As k is increased from 0.01 to 1.10, the dp/dz profile is shifted dramatically upwards in the line plot (left panel), rendering it less favorable (more positive or less negative). The contour plot (center panel) shows how dp/dz changes with z and k meaning the effect is uniform along the channel. The surface plot (right panel) shows a three-dimensional perspective, and makes it very clear how the entire surface of the pressure gradient rises with increasing k. The physical interpretation is simple: The higher the k, the greater the Darcy damping term $-k\mu w$ in the momentum equation that resists the fluid motion. To compensate for this extra resistance, the pressure gradient has to become less favorable for the flow to keep the same flow rate (i.e., the pressure increases). The parameter k has the greatest effect on dp/dz, which is a competitor to the effects of ω_e and Q.

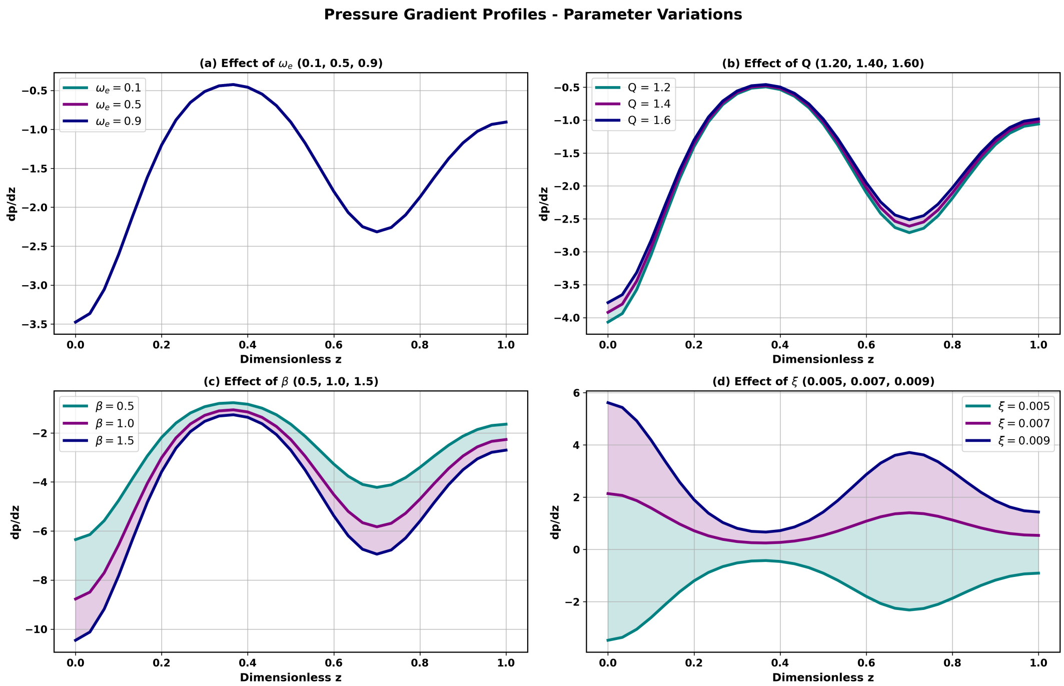

Figure 12. Pressure gradient profiles dp/dz along the dimensionless axial coordinate z for Model I (Carreau-Yasuda) showing the influence of (a) Weissenberg number ω_e, (b) heat source parameter Q, (c) first-order slip parameter β, and (d) second-order slip parameter ξ. In each panel, the indicated parameter is varied, while all others are held at the baseline values $k = 0.01$, $R_e = 0.1$, $G_r = 3.0$, $G_f = 5.0$, $Pr = 0.7$, $Ec = 0.9$, $N_b = 3.1$, $N_t = 0.1$, $Q = 2.0$, $\gamma_{\text{abs}} = 0.5$, $Rm = 3.0$, $S = 2.5$, $\beta = 0.1$, $\xi = 0.005$, and $\omega_e = 0.01$, over the domain $r \in [0.2, 1.6]$ at fixed flow rate $q = 2.0$ ($N = 161$). The oscillatory shape of dp/dz reflects the wavy outer-wall geometry $R_2(z)$; shaded regions indicate the range of variation between the plotted parameter values.

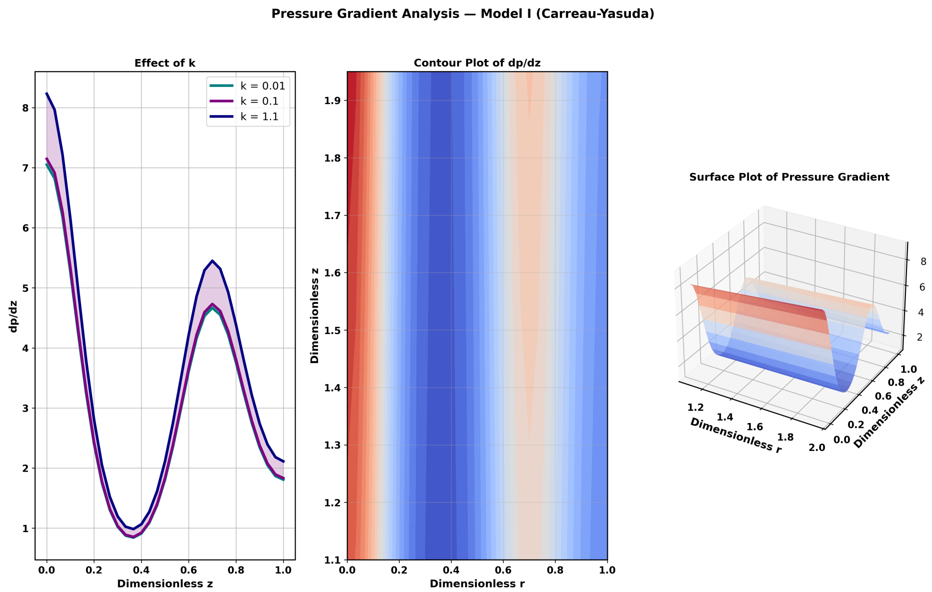

Figure 13. Pressure gradient analysis for the porous parameter k, showing (a) line plots of dp/dz along z for $k = 0.01$, 0.10, and 1.10, (b) a contour plot, and (c) a three-dimensional surface plot of $dp/dz(z, k)$.

5.5. Practical implications for nanoparticle-based drug delivery

The coupled transport picture developed above translates into several concrete design principles for intra-articular nanoparticle therapy. First, cartilage absorption emerges as the primary barrier to delivery: the absorption sink $-\gamma_{\text{abs}}\phi$ markedly lowers the near-wall nanoparticle concentration and the associated wall gradient, so a substantial fraction of an injected dose is taken up before it can distribute through the synovial space. This suggests that bioavailability is improved less by increasing the injected quantity than by slowing uptake, for example, through surface modification (such as PEGylation) or through delivery schedules that transiently saturate the near-wall region [7].

Second, thermophoresis provides an actively controllable means of steering particles. Because the concentration field responds strongly to the imposed temperature gradient, and because gold nanoparticles can be heated photothermally, the same particles that carry the drug can, in principle, be used to reshape their own spatial distribution [8, 9]. Thermophoretic migration therefore represents a lever for guiding nanoparticles toward, or away from, the articular surface rather than relying on passive diffusion alone.

Third, the interplay of viscous and internal heating defines a design window for photothermal activation. Heating is a useful actuator for release and steering, but the temperature elevations associated with cyclic loading and internal sources must remain below the threshold at which catabolic enzyme activity and proteoglycan degradation are promoted [19, 20]. The present model provides a framework for bounding safe activation levels rather than a specific dose.

Finally, the sensitivity of the induced magnetic field to surface slip points to a possible non-invasive diagnostic dimension: Because transport and its electromagnetic signature depend on the state of the cartilage surface, which degrades in osteoarthritis, delivery performance is expected to differ between healthy and diseased joints, and surface condition may in principle be inferred without arthrocentesis.

Consistent with the modeling scope of this study, these implications are offered as mechanistic design principles and testable hypotheses for future experimental work rather than as quantitative in-vivo predictions.

6. Conclusions

This study examined the coupled transport of momentum, heat, nanoparticles, and an induced magnetic field in a wavy, porous channel representing the knee joint, with the aim of understanding how these processes shape the distribution of gold nanoparticles for drug delivery. The problem is clinically pressing: osteoarthritis affects some 500 million people worldwide, and current viscosupplementation therapies clear quickly and penetrate cartilage poorly. To study this, we developed a Python-based finite volume solver incorporating three non-Newtonian viscosity models, a novel absorption term $-\gamma_{\text{abs}}\phi$ in the concentration equation, and a second-order slip condition $w = 1 - \beta(\partial w/\partial r) - \xi(\partial^2 w/\partial r^2)$ at the wavy outer wall. The oscillatory pressure gradient was recovered directly by linear superposition, without an iterative solver.

A consistent picture emerges from the results: Rather than one parameter governing everything, each transport process is led by a distinct mechanism. The velocity field is set primarily by thermal buoyancy (G_r) and the second-order slip coefficient ξ, whose contributions are comparable and clearly outweigh those of porous drag and magnetic force. Temperature is governed mainly by viscous dissipation (Ec) and the internal heat source Q. Nanoparticle concentration is limited above all by cartilage absorption (γ_{abs}), while thermophoresis (N_t) is the principal means of steering particles once they are in suspension. The axial pressure gradient depends chiefly on cartilage permeability (k) and fluid rheology (ω_e), and is largely unaffected by first-order slip (β). The induced magnetic field rises monotonically with both surface slip and the magnetic Reynolds number; because its absolute magnitude is sensitive to numerical resolution, we report it as a trend rather than a fixed value. The main conclusions follow.

- Second-order slip (ξ) is a leading-order control on flow in wavy geometries, producing a velocity enhancement comparable to that of thermal buoyancy, yet it is routinely left out of biomedical flow models.
- Cartilage absorption (γ_{abs}) is the dominant barrier to delivery, markedly lowering the near-wall nanoparticle concentration over the range studied; slowing this uptake, for instance through surface modification, could therefore improve bioavailability.
- Thermophoresis (N_t) offers a tunable route to actively direct nanoparticles, one that the photothermal response of gold makes practically accessible, while viscous dissipation (Ec) is the primary lever on intra-articular temperature.
- The induced magnetic field is strongly sensitive to fluid viscoelasticity and surface slip, but largely indifferent to thermal and concentration parameters, which points, in principle, to a non-invasive means of probing cartilage-surface condition.
- The pressure distribution is set by cartilage permeability (k) and fluid rheology (ω_e) rather than by wall slip (β).

The novelty of the work rests on four contributions: a Carreau-Yasuda model coupled to both temperature and concentration; a second-order slip condition in a wavy, porous geometry; an absorption/desorption term in the concentration equation; and a full magnetic-induction treatment of the induced field. Together, these results show that second-order slip, nanoparticle absorption, and induced-field generation are not negligible in predictive models of synovial joint biomechanics, and they establish qualitative benchmarks, the dominance of slip and buoyancy in the flow, of absorption in mass transfer, and of viscous dissipation in the thermal field, against which future experimental and computational studies can be assessed.

Limitations and future work:

Several limitations of the present study should be noted. First, the model has been validated against an exact analytical solution in a reduced limit and benchmarked against prior computational work, but no direct experimental validation is currently possible, as experimental data for this specific coupled configuration (magnetohydrodynamic gold-nanoparticle synovial flow with second-order slip and an induced field) are not yet available; experimental measurement of the predicted transport trends is an important direction for future work. Second, several dimensionless groups, notably the Eckert, magnetic Reynolds, and Strommer numbers, are treated as representative model parameters rather than in-vivo magnitudes, so the corresponding results are interpreted as qualitative trends rather than quantitative physiological predictions. Third, the second-order slip coefficient and the absorption coefficient are not yet experimentally constrained for articular cartilage and are therefore varied parametrically; their measurement would allow the model to be calibrated to specific joints. Fourth, the absorption process is represented as a homogenized first-order volumetric sink, appropriate in the dilute limit; a wall-resolved, saturable (e.g., Langmuir-type) uptake model would be a natural refinement. Finally, the Prandtl number is adopted as a standard modeling value rather than a physiological property of synovial fluid, whose effective value is higher and shear-dependent. Future work will address these points through experimental calibration, saturable absorption kinetics, and physiologically grounded parameter estimation.

Author contributions

All authors contributed equally to the writing and analysis of the manuscript. All authors have read and approved the final version of the manuscript for publication.

Use of Generative-AI tools declaration

The authors declare they have not used Artificial Intelligence (AI) tools in the creation of this paper.

Acknowledgments

The authors extend their appreciation to the Deanship of Scientific Research at Northern Border University, Arar, KSA for funding this research work through the project number NBU-FPEJ-2026-2090-01.

Conflicts of interest

The authors declare that they have no competing interests.

References

1. G. Musumeci, The effect of mechanical loading on articular cartilage, *J. Funct. Morphol. Kinesiol.*, **1** (2016), 154–161. https://doi.org/10.3390/jfmk1020154
2. B. Kurz, T. Lange, M. Voelker, M. L. Hart, B. Rolauffs, Articular cartilage–from basic science structural imaging to non-invasive clinical quantitative molecular functional information for AI classification and prediction, *Int. J. Mol. Sci.*, **24** (2023), 14974. https://doi.org/10.3390/ijms241914974
3. N. Ouerfelli, N. Vrinceanu, E. Mliki, K. A. Amin, L. Snoussi, D. Coman, et al., Rheological behavior of the synovial fluid: a mathematical challenge, *Front. Mater.*, **11** (2024), 1386694. https://doi.org/10.3389/fmats.2024.1386694
4. A. Ruggiero, Milestones in natural lubrication of synovial joints, *Front. Mech. Eng.*, **6** (2020), 52. https://doi.org/10.3389/fmech.2020.00052
5. F. Cao, Z. W. Xu, X. X. Li, Z. Y. Fu, R. Y. Han, J. L. Zhang, et al., Trends and cross-country inequalities in the global burden of osteoarthritis, 1990–2019: a population-based study, *Ageing Res. Rev.*, **99** (2024), 102382. https://doi.org/10.1016/j.arr.2024.102382
6. M. Pigeolet, A. Jayaram, K. B. Park, J. G. Meara, Osteoarthritis in 2020 and beyond, *Lancet*, **397** (2021), 1059–1060. https://doi.org/10.1016/S0140-6736(21)00208-7
7. X. Li, B. Y. Dai, J. X. Guo, L. Z. Zheng, Q. Y. Guo, J. Peng, et al., Nanoparticle-cartilage interaction: pathology-based intra-articular drug delivery for osteoarthritis therapy, *Nano-Micro Lett.*, **13** (2021), 149. https://doi.org/10.1007/s40820-021-00670-y
8. S. Rasmussen, C. Frederickson, G. Danscher, Inhibition of local inflammation by implanted gold: a narrative review of the history and use of gold, *J. Rheumatol.*, **50** (2023), 704–705. https://doi.org/10.3899/jrheum.221150
9. G. Danscher, S. Rasmussen, NanoGold and μGold inhibit autoimmune inflammation: a review, *Histochem. Cell Biol.*, **159** (2023), 225–232. https://doi.org/10.1007/s00418-023-02182-9
10. Y. Deng, B. Li, H. Zheng, L. Liang, Y. P. Yang, S. Q. Liu, et al., Multifunctional Prussian blue nanoparticles loading with Xuetongsu for efficient rheumatoid arthritis therapy through targeting inflammatory macrophages and osteoclasts, *Asian J. Pharm. Sci.*, **20** (2025), 101037. https://doi.org/10.1016/j.ajps.2025.101037
11. T. Hayat, B. Ahmed, F. M. Abbasi, A. Alsaedi, Numerical investigation for peristaltic flow of Carreau-Yasuda magneto-nanofluid with modified Darcy and radiation, *J. Thermal Anal. Calorim.*, **137** (2019), 1359–1367. https://doi.org/10.1007/s10973-019-08018-w
12. S. M. Kayani, S. Hina, M. Mustafa, A new model and analysis for peristalsis of Carreau-Yasuda (CY) nanofluid subject to wall properties, *Arab. J. Sci. Eng.*, **45** (2020), 5179–5190. https://doi.org/10.1007/s13369-020-04359-z
13. A. Coclite, G. M. Coclite, D. De Tummasi, Capsules rheology in Carreau-Yasuda fluids, *Nanomaterials*, **10** (2020), 2190. https://doi.org/10.3390/nano10112190

14. P. Bitla, F. Y. Sitotaw, Hydromagnetic flow of two immiscible couple stress fluids in an inclined porous channel: effects of slip boundary, *Math. Probl. Eng.*, **2023** (2023), 9683532. https://doi.org/10.1155/2023/9683532

15. M. Nazeer, A. A. Al Ahamdi, A. N. Alzaed, M. Alwetaishi, M. W. Nazir, M. I. Khan, Impact of slip boundary conditions, magnetic force, and porous medium on blood flow of jeffrey fluid, *Z. Angew. Math. Mech.*, **102** (2022), e202100218. https://doi.org/10.1002/zamm.202100218

16. Y. Akbar, S. Huang, A. Magesh, J. Ji, M. M. Alam, Thermal analysis of mixed convective peristaltic pumping of nanofluids in the occurrence of an induced magnetic field and variable viscosity, *J. Taibah Univ. Sci.*, **18** (2024), 2319890. https://doi.org/10.1080/16583655.2024.2319890

17. U. Farooq, A. Jan, M. Hussain, Impact of thermal radiations, heat generation/absorption and porosity on MHD nanofluid flow towards an inclined stretching surface: non-similar analysis, *Z. Angew. Math. Mech.*, **104** (2024), e202300306. https://doi.org/10.1002/zamm.202300306

18. S. Akram, M. Athar, K. Saeed, A. Razia, T. Muhammad, H. A. Alghamdi, Mechanism of double-diffusive convection on peristaltic transport of thermally radiative Williamson nanomaterials with slip boundaries and induced magnetic field: a bio-nanoengineering model, *Nanomaterials*, **13** (2023), 941. https://doi.org/10.3390/nano13050941

19. M. N. Moghadam, P. Abdel-Sayed, V. M. Camine, D. P. Pioletti, Impact of synovial fluid flow on temperature regulation in knee cartilage, *J. Biomech.*, **48** (2015), 370–374. https://doi.org/10.1016/j.jbiomech.2014.11.008

20. P. Abdel-Sayed, M. N. Moghadam, R. Salomir, D. Tchernin, D. P. Pioletti, Intrinsic viscoelasticity increases temperature in knee cartilage under physiological loading, *J. Mech. Behav. Biomed. Mater.*, **30** (2014), 123–130. https://doi.org/10.1016/j.jmbbm.2013.10.025

21. J. Buongiorno, Convective transport in nanofluids, *J. Heat Transfer*, **128** (2006), 240–250. https://doi.org/10.1115/1.2150834

22. S. Rehman, A. Farooq, M. A. Iqbal, Neuro-heuristic and regression-based modeling of three-dimensional williamson-micropolar nanofluid flow with regularization and uncertainty quantification, *Eng. Appl. Artif. Intell.*, **166** (2026), 113667. https://doi.org/10.1016/j.engappai.2025.113667

23. A. Farooq, S. Rehman, W. X. Ma, Comparative study of regression-based data-driven models for thermally stratified Carreau nanofluids with magnesium oxide nanoparticles, *Phys. Fluids*, **37** (2025), 082032. https://doi.org/10.1063/5.0274063

24. B. M. J. Rana, S. Islam, M. Y. Ali, M. M. Molla, Exploring microbial dynamics and heat transmission in a nonlinear radiative Maxwell nanomaterial with sensitivity analysis, *Adv. Math. Phys.*, **2025** (2025), 8544390. https://doi.org/10.1155/admp/8544390

25. T. Islam, B. M. J. Rana, M. Y. Ali, K. E. Hossain, A. Mukherjee, S. Islam, et al., Artificial neural network modeling of magnetic nanoparticle-enhanced Sisko blood nanofluid flow over an inclined stretching surface with non-uniform heating and thermophoretic effects, *Int. J. Thermofluids*, **31** (2026), 101542. https://doi.org/10.1016/j.ijft.2025.101542

26. S. V. Patankar, *Numerical heat transfer and fluid flow*, Hemisphere Publishing Corporation, 1980.

27. H. K. Versteeg, W. Malalasekera, *An introduction to computational fluid dynamics: the finite volume method*, Pearson Education, 2007.

28. S. F. Ramadan, K. S. Mekheimer, M. M. Bhatti, C. M. Khalique, Induced magnetic field and thermal regulation of synovial fluid flow through irregular surfaces with first-order slip and gold nanoparticles, *Sep. Sci. Technol.*, **60** (2025), 133–156. https://doi.org/10.1080/01496395.2024.2418290

29. S. Bashir, M. Ramzan, J. D. Chung, Y. M. Chu, S. Kadry, Analyzing the impact of induced magnetic flux and Fourier's and Fick's theories on the Carreau-Yasuda nanofluid flow, *Sci. Rep.*, **11** (2021), 9230. https://doi.org/10.1038/s41598-021-87831-6

30. K. Javid, N. Ali, Z. Asghar, Numerical simulation of the peristaltic motion of a viscous fluid through a complex wavy non-uniform channel with magnetohydrodynamic effects, *Phys. Scr.*, **94** (2019), 115226. https://doi.org/10.1088/1402-4896/ab2efb

31. J. C. Misra, S. K. Pandey, Peristaltic transport of physiological fluids, In: *Biomathematics: Modelling and simulation*, World Scientific, 2006, 167–193. https://doi.org/10.1142/9789812774859_0007

32. R. B. Bird, W. E. Stewart, E. N. Lightfoot, *Transport phenomena*, John Wiley & Sons, 2007.

33. N. O. Al-Atawi, S. Hasnain, M. Saqib, D. S. Mashat, Significance of Brinkman and Stokes system conjuncture in human knee joint, *Sci. Rep.*, **12** (2022), 18992. https://doi.org/10.1038/s41598-022-23402-7

34. G. N. Hao, R. Yu, X. W. Dong, Z. N. Li, Simulation of droplet impacting on elastic pillars using smoothed particle hydrodynamics method, *J. Fluids Struct.*, **143** (2026), 104541. https://doi.org/10.1016/j.jfluidstructs.2026.104541

35. I. B. Celik, U. Ghia, P. J. Roache, C. J. Freitas, Procedure for estimation and reporting of uncertainty due to discretization in CFD applications, *J. Fluids Eng.*, **130** (2008), 078001. https://doi.org/10.1115/1.2960953

AIMS Press